Memory-induced nonlinear dynamics of excitation in cardiac diseases

Julian Landaw and Zhilin Qu

Memory-induced nonlinear dynamics of excitation in cardiac diseases

Julian Landaw and Zhilin Qu*

Department of Medicine (Cardiology), University of California, Los Angeles, California 90095, USA and
Department of Biomathematics, University of California, Los Angeles, California 90095, USA

(Dated: April 3, 2018)

Excitable cells, such as cardiac myocytes, exhibit short-term memory, i.e., the state of the cell depends on its history of excitation. Memory can originate from slow recovery of membrane ion channels or from accumulation of intracellular ion concentrations, such as calcium ion or sodium ion concentration accumulation. Here we examine the effects of memory on excitation dynamics in cardiac myocytes under two diseased conditions, early repolarization and reduced repolarization reserve, with memory from two different sources: slow recovery of a potassium ion channel and slow accumulation of the intracellular calcium ion concentration. We first carry out computer simulations of action potential models described by differential equations to demonstrate complex excitation dynamics, such as chaos. We then develop novel iterated map models that incorporate memory, which accurately capture the complex excitation dynamics and bifurcations of the action potential models. Finally, we carry out theoretical analyses of the iterated map models to reveal the underlying mechanisms of memory-induced nonlinear dynamics. Our study demonstrates that the memory effect can be unmasked or greatly exacerbated under certain diseased conditions, which promotes complex excitation dynamics, such as chaos. The iterated map models reveal that memory converts a monotonic iterated map function into a nonmonotonic one to promote the bifurcations leading to high-periodicity and chaos.

PACS numbers: 05.45.-a, 87.15.A-, 87.19.Hh

I.   INTRODUCTION

Dynamical instabilities in the heart can promote arrhythmias such as ventricular tachycardia and fibrillation (VT/VF)[1, 2], which are the leading causes of sudden cardiac death [3]. Different mechanisms of dynamical instabilities have been demonstrated at both single-cell and tissue scales [4–6]. In single cells, nonlinear dynamics including period-doubling bifurcations leading to period-2 (called alternans in cardiac electrophysiology) and other states of higher periodicity, as well as quasiperiodicity and chaos have been widely demonstrated [7–13]. These dynamics originate from the nonlinearity in membrane voltage, intracellular calcium (Ca^{2+}) cycling, or coupling of the two [6, 14].

Low-dimensional iterated maps have been widely used to understand the dynamical mechanisms of complex cardiac excitations. The earliest and most widely used iterated map model was based on action potential (AP) duration (APD) restitution properties of cardiac myocytes [7]. APD restitution is a property well-known in cardiology and widely measured in experiments [15–19]. One type of APD restitution is called the S1S2 APD restitution (see Fig. 1(a)), in which the cell is periodically paced (S1) to a steady state and then a premature or delayed stimulus (S2) is applied to obtain the dependence of APD on the preceding diastolic interval (DI). The S1S2 APD restitution can be mathematically defined as

$$a_{n+1} = f(d_n), \tag{1}$$

where a_{n+1} is the APD of the $(n + 1)^{st}$ beat and d_n is the DI of the nth beat (immediately preceding a_{n+1}). Under periodic pacing, the APD and DI of the same beat satisfy the relation $a_n + d_n = mT$, and so Eq. (1) can be rewritten as

$$a_{n+1} = f(mT - a_n), \tag{2}$$

where T is the pacing period and mT is the actual excitation period. For example, $m = 1$ indicates that every stimulus gives rise to an AP (1:1 capture), $m = 2$ means every two stimuli result in an AP (2:1 capture), and so on. Eq. (2) or similar ones have been widely used to investigate APD dynamics under periodic stimulation [7, 9–12, 20–22]. A period-doubling bifurcation occurs when the slope of the APD-restitution curve at the fixed point exceeds 1. Chaos may occur when f is either a nonmonotonic function of DI or a monotonic function with stimulation failure [22]. In this study, we refer to Eq. (2) as the "APD-restitution map model."

Note that in Eq. (1), the APD depends only on its immediately preceding DI, indicating no memory. However, cardiac systems exhibit memory [15, 23, 24], in which the APD depends not only on its immediately preceding DI, but also on earlier APDs and DIs. Therefore, Eq. (2) is no longer accurate or valid to describe the APD dynamics when memory is present. A higher-dimensional iterated map is needed to incorporate the memory effect. In general, one can write

$$a_{n+1} = f(d_n, a_n, d_{n-1}, a_{n-1}, \dots), \tag{3}$$

and use this map to investigate the nonlinear dynamics caused by memory [25]. Another way of incorporating memory into the iterated map model is to induce phenomenologically a memory variable. One such model was

developed by Chialvo *et al.* [26] and Fox *et al.* [27], which is described by the following equations:

$$M_{n+1} = e^{-\frac{d_n}{\tau}} \left[1 - (1 - M_n)e^{-\frac{a_n}{\tau}} \right] \qquad (4)$$

$$a_{n+1} = (1 - \alpha M_{n+1})f(d_n) \qquad (5)$$

where M is the memory variable and τ is the time constant of memory. M in Eq. (4) describes the memory effect mainly from the slow recovery of K^+ channels. In a study by Schaeffer *et al.* [28], an iterated map model was developed to describe the memory effect from slow intracellular ion accumulation. Since M is always positive, the steepness of the restitution function in Eq. (5) is reduced, and thus memory in Eqs. (4) and (5) always suppresses instability [26, 27]. The effects of memory on cardiac excitation dynamics have been investigated in many other previous studies [25, 29–37], which have also shown that memory suppresses dynamical instabilities.

In a recent study [38], we showed that under certain diseased conditions, memory can induce dynamical instabilities and complex APD dynamics. One such diseased condition is the presence of a strong transient outward potassium (K^+) current (I_{to}), which can cause a sudden shortening of APD, the so-called spike-and-dome AP morphology [39–41] (also see Fig. 2(a)). I_{to} can induce complex APD dynamics, including alternans and high periodicity as well as chaos, which have been shown in experiments [42] and computer simulations [43–46]. This condition may occur under cardiac diseases such as Brugada syndrome and ischemia [42, 47]. Another condition we studied is the condition of reduced repolarization reserve in which either the outward currents are reduced or the inward currents are increased from normal conditions. This causes the lengthening of APD and the genesis of early afterdepolarizations (EADs) [48, 49]. This condition may occur in cardiac diseases such as long QT syndrome [50–53] and heart failure [54]. In our previous study [38], we carried out computer simulations using a simplified AP model, the 1991 Luo and Rudy (LR1) model [55], to simulate the complex APD dynamics under the two conditions. We developed a novel iterated map model which accurately captures the dynamics from the AP model and revealed the mechanistic role of memory in promoting these dynamics. This is contrary to the understanding of the memory effects on cardiac excitation dynamics from previous studies [25–27, 29–37] which have shown that memory suppresses dynamical instabilities.

In this study, we extend our previous work to investigate the effects of memory on APD dynamics. We investigate two sources of memory. In the first one, memory is from the slow recovery of a K^+ channel. In the second one, memory is from the slow accumulation of intracellular ion concentrations. Since the LR1 model does not have intracellular ion concentration dynamics (they are fixed), we use the model developed by ten Tusscher *et al.* [56], the TP04 model, to study the effects of memory due to ion concentration accumulation, namely intra-

cellular Ca^{2+} concentration ($[Ca^{2+}]_i$) accumulation. We first carry out computer simulations of the AP models to demonstrate bifurcations and complex APD dynamics under the two diseased conditions. We then develop iterated map models that incorporate memory to accurately capture the complex dynamics and bifurcations. Finally, we perform theoretical analyses of the iterated map models to reveal the underlying mechanisms and the roles of memory in promoting the complex dynamics.

The article is organized as follows. In *Section II*, we describe the AP models, namely the LR1 model and the TP04 model, and our modifications to model the diseased conditions that exhibit the corresponding APD dynamics. The Results section, *Section III*, is divided into two major sections based on the two sources of memory. *Section A* investigates the effects of memory originating from the slow recovery of K^+ channels. We choose to use the LR1 model since it does not exhibit ion accumulation, so memory originates only from slow ion channel recovery. In *Section A.1*, we add I_{to} to the LR1 model to model Brugada syndrome and show that I_{to} can unmask or greatly exacerbate the memory effect caused by slow recovery of the time-dependent K^+ current (I_K). In *Section A.2*, we show that adding I_{to} to the LR1 model can give rise to complex APD dynamics, including alternans and chaos, which cannot be described by the traditional iterated map model using the S1S2 APD restitution curve. In *Section A.3*, we develop a new iterated map model that incorporates the memory effect from the slow recovery of I_K. Since the memory is mainly determined by the slow kinetics of the $X-$gating variable, we call the new iterated map model the "X-memory map model." In *Section A.4*, we show that the $X-$memory map model can accurately capture the complex APD dynamics from the AP model and the presence of memory results in a nonmonotonic first return map to generate chaos. In *Section A.5*, we perform a stability analysis of the $X-$memory map model, investigating the dependence of the APD dynamics on different parameters, and validate some of the predictions using the AP model. In *Section A.6*, we investigate the second diseased condition, long QT syndrome, in which inward currents are increased and/or outward currents are reduced. We show that memory is also unmasked or exacerbated and the resulting complex APD dynamics cannot be accurately captured by the traditional APD-restitution map model. On the other hand, the $X-$memory map model can accurately capture bifurcations and the complex APD dynamics from the AP model.

Section B investigates the effects of memory originating from slow $[Ca^{2+}]_i$ accumulation. We choose to use the TP04 model since it exhibits slow ion accumulation but its ion channel recovery is fast. Following the same approach as in *Section A*, we simulated the two diseased conditions: adding I_{to} to simulate Brugada syndrome, and increasing inward currents and reducing outward currents to simulate long QT syndrome. We develop a new iterated map model that incorporates the mem-

ory effects from slow $[\mathrm{Ca}^{2+}]_i$ accumulation, and call this model the "$\mathrm{Ca}^{2+}-$memory map model." We show that the traditional APD-restitution map model cannot while the $\mathrm{Ca}^{2+}-$memory map model can accurately capture the bifurcations and the complex APD dynamics from the AP model. In the final section, *Section IV*, we discuss briefly the implications of our findings from the AP models and the new iterated map models to cardiac arrhythmogenesis and potential applications to other excitable systems.

II. ACTION POTENTIAL MODELS AND SIMULATION METHODS

We carry out computer simulations using two AP models with the voltage (V) governed by the following differential equation:

$$C_m \frac{dV}{dt} = -I_{\mathrm{ion}} + I_{\mathrm{sti}}, \qquad (6)$$

where $C_m = 1\,\mu\mathrm{F/cm}^2$ is the membrane capacitance, I_{ion} is the total ionic current density, and I_{sti} is the stimulus current density, a square pulse for a set duration of time. I_{ion} is the sum of the ionic currents, each driven by the flow of Na^+, K^+, and/or Ca^{2+} flowing in and out of the cell. The number of individual currents and their mathematical formulations depend on specific AP models. The first model we use is the LR1 model [55], which is one of the simplest cardiac AP models with physiological ionic current formulations. In this model, we use $I_{\mathrm{sti}} = 80\,\mu\mathrm{A/cm}^2$ with a 0.5 ms duration. The second model we use is a much more complex one, a human ventricular AP model developed by ten Tusscher *et al.*[56]. In this model, we use $I_{\mathrm{sti}} = 52\,\mu\mathrm{A/cm}^2$ with a 1 ms duration.

Since there is no I_{to} in the LR1 model, we include an I_{to} current taken from the model by Mahajan *et al.* [57],

$$I_{to} = g_{to} x_{to} y_{to} (V - E_K), \qquad (7)$$

where g_{to} is the maximum conductance, x_{to} is the activation gating variable, y_{to} is the inactivation gating variable, and E_K is the reversal potential of the K^+ channel. We take the formulation of the fast I_{to} (i.e., $I_{to,f}$) from the Mahajan *et al.* model. I_{to} formulations (both slow and fast I_{to}) are present in the TP04 model. For simplicity and consistency, we remove the two original I_{to} formulations and added the above I_{to} formulation (Eq. (7)) to the TP04 model.

A time-adaptive forward-Euler method is used in computer simulations. The time step is $\Delta t = 0.05$ ms if the change in voltage $\Delta V < 0.1$ mV, otherwise the time step is $\Delta t = 0.005$ ms. The cell is paced periodically with period T.

III. RESULTS

A. Complex APD Dynamics Caused by Memory Originating from Slow Recovery of Ion Channels

We first investigate the effects of memory originating from slow recovery of membrane ion channels. During an AP, ion channels activate and then inactivate/deactivate, and after the AP it takes a certain amount of time for the ion channels to fully recover. Different ion channels have different recovery times, ranging from a few milliseconds to seconds or even longer. Memory manifests from slowly recovering ion channels. One potential source of memory is the slow component of the delayed rectifier K^+ current (I_{Ks}) [58–60], which activates and recovers slowly, on the order of several hundred milliseconds to a couple seconds. In this section, we use the LR1 model to investigate the effects of memory induced by slow K^+ channel recovery. Since the ion concentrations are fixed in the LR1 model, one avoids the confluent effects of memory caused by slow ion accumulation. In the LR1 model, the time-dependent K^+ current (I_K) is a slowly activating and recovering current.

1. Memory unmasked/exacerbated by I_{to}

To demonstrate the effects of I_{to} on memory, we plot S1S2 APD restitution curves of the AP model with and without I_{to} for different S1 pacing periods, T_{S1S1} (see Fig. 1(a) for the S1S2 pacing protocol). The difference in APD restitution as a result of applying different pre-pacing S1S1 intervals is a measure of the memory effect [30].

Fig. 1(b) shows S1S2 APD restitution curves of the original LR1 model for two different S1 pacing periods $T_{S1S1} = 400$ ms and 1000 ms. The shorter S1 pacing period results in an APD restitution curve that shifts slightly to the right. Thus, in the LR1 model without I_{to}, the effect of memory on APD restitution is small.

The presence of I_{to} causes significant changes in AP morphology and the resulting APD restitution curves. I_{to} is an outward K^+ current that spikes during phase-1 and is almost completely inactivated during phase-2 (Figs. 2(a) and (b)). Fig. 2(c) demonstrates the effects on AP morphology by I_{to}. In the original model (solid/black trace in 2(c)), the phase-1 notch of the AP terminates at roughly 10 mV. I_{to} causes a more pronounced phase-1 notch. If the I_{to} conductance is larger than a critical value, the voltage repolarizes immediately after the notch, resulting in early repolarization without a phase-2 plateau, known as a spike (dashed/red trace in 2(c)). If the I_{to} conductance is smaller than the critical value, there is a rebound depolarization during phase-2, known as a spike-and-dome (short-dashed/blue trace in 2(c)).

I_{to} creates an "all-or-none" behavior leading to so-called spike-and-dome AP morphology, in which small changes in I_{to} conductance result in either a spike-and-
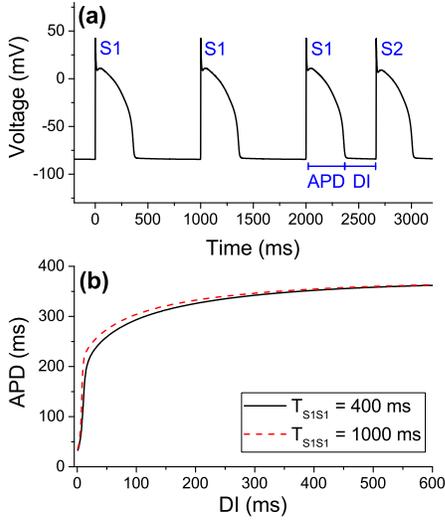
FIG. 1. The S1S2 restitution protocol and S1S2 APD restitution curves from the original LR1 model. **(a)**. APs demonstrating the S1S2 restitution protocol. Here, $T_{S1S1} = 1000$ ms, and the S2 stimulus is applied after the third S1 beat with a diastolic interval DI = 300 ms. **(b)**. Restitution curves showing the dependence of APD on DI for different S1 pacing periods $T_{S1S1} = 400$ ms (solid/black) and $T_{S1S1} = 1000$ ms (dashed/red). Note that the two curves differ only slightly, indicating a small memory effect.

dome with a long APD or a spike with a short APD, as seen in the short-dashed/blue and dashed/red APs in Fig. 2(c). Fig. 2(d) shows this sensitive dependence of APD on g_{to}, the maximum conductance of I_{to}. Increasing g_{to} initially decreases APD slightly, then increases APD up to about 500 ms, at which point APD decreases sharply from 500 ms down to 100 ms. Fig. 2(e) reveals the effects of I_{to} on the restitution curves in the presence of varying levels of g_{to}. The presence of I_{to} causes the restitution curve to have a more sensitive dependence on DI. In particular, there is a critical value of DI where the dependence of APD is very steep. As g_{to} increases, the APD restitution curves shift to the right.

Fig. 2(f) reveals the effect of changing the S1 pacing period, from $T_{S1S1} = 400$ ms to 2000 ms. The longer S1 pacing period causes the APD restitution curve to shift significantly to the right by about 300 ms. Compare this to the case without I_{to} (Fig. 1(b)), where instead the shorter pacing period causes a very slight shift to the right and by only a few milliseconds. This indicates that in the presence of I_{to}, there is a significant effect of memory. Since the I_{to} formulation we added to the LR1 model is the fast I_{to}, the time constants are small, typically less than 100 ms, and thus memory is not directly from I_{to} itself. The memory still originates from the slow recovery of I_K, but I_{to} unmasks and exacerbates the memory effect, causing a large effect on S1S2 APD restitution behaviors.
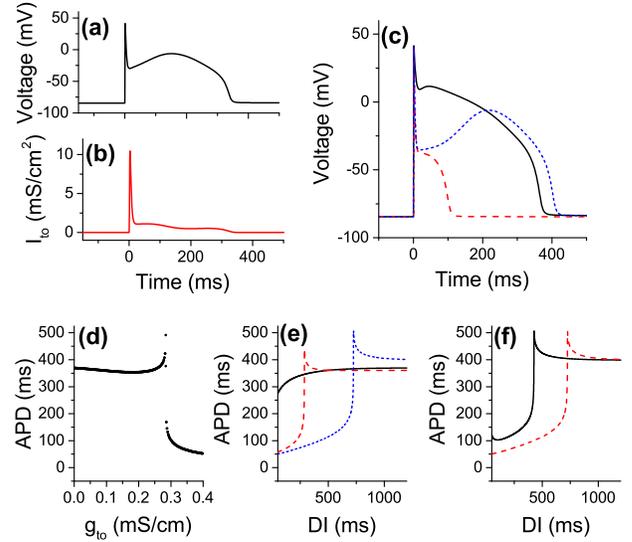

FIG. 2. The effects of I_{to} on AP morphology and APD. **(a)**. AP with a pronounced phase-1 notch. **(b)**. I_{to} activity during the AP in (a). **(c)**. APs in the absence of I_{to} (solid/black) and in the presence of I_{to} inducing a spike (dashed/red, $g_{to} = 0.3$ mS/cm^2) and spike-and-dome (short-dashed/blue, $g_{to} = 0.28$ mS/cm^2). **(d)**. Dependence of APD on g_{to}. The pacing period is $T = 2000$ ms. Initially, increasing g_{to} decreases APD, then increases APD up to a critical value when APD = 500 ms, at which point an increase in g_{to} causes a sudden drop in APD to 100 ms. **(e)**. Dependence of APD restitution curves on g_{to}. The S1 pacing period is $T_{S1S1} = 2000$ ms. Without I_{to} (solid/black), the restitution curve is flat except for DI < 200 ms. With I_{to} (dashed/red and short-dashed/blue), there is a sensitive dependence of APD around a critical value of DI. The higher value of g_{to} (short-dashed/blue, $g_{to} = 0.278$ mS/cm^2) causes a restitution curve that is right-shifted from that of the lower value (dashed/red, $g_{to} = 0.24$ mS/cm^2). **(f)**. Dependence of APD restitution curves on the S1 pacing period T_{S1S1}, in the presence of I_{to} with $g_{to} = 0.278$ mS/cm^2. $T_{S1S1} = 400$ ms for solid/black trace, 2000 ms for dashed/red trace. We use $T_{S1S1} = 2000$ ms instead of 1000 ms (as in Fig. 1) in order to avoid alternans during S1 pacing.

2. $I_{to}-$induced complex APD dynamics

We next demonstrate how APD dynamics are effected by I_{to}. In the prior section, we showed that in the absence of I_{to}, the S1S2 restitution curves remain nearly identical when the S1 pacing period is either $T_{S1S1} = 400$ ms or 1000 ms. Using the APD-restitution map model (Eq. (2)), where the function f is numerically obtained by using the S1S2 APD restitution curves from the simulation of the LR1 model (e.g. from Fig. 1(b)), we can obtain the bifurcation diagrams showing the global APD dynamics captured by the restitution map.
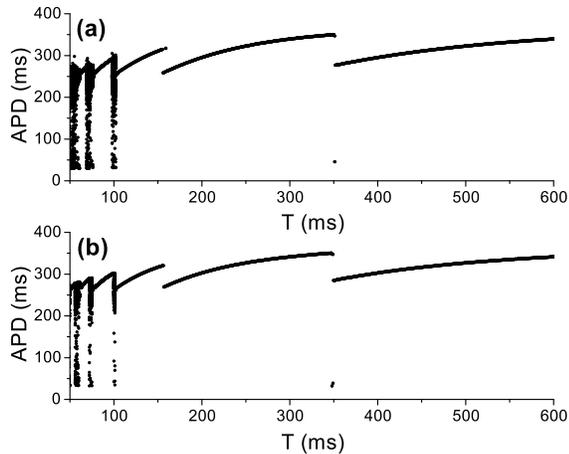
The bifurcation diagrams generated from the AP

FIG. 3. APD dynamics of the LR1 model in the absence of I_{to}. **(a)**. Bifurcation diagram of the AP model under constant-T pacing. **(b)**. Bifurcation diagram generated from the APD-restitution map model (Eq. (2)) using the S1S2 APD restitution curve with $T_{S1S1} = 1000$ ms (dashed/red curve in Fig. 1(b)). The two diagrams are nearly identical.

model (Fig. 3(a)) and generated from Eq. (2) using the APD restitution curve for $T_{S1S1} = 1000$ ms in 1(b) (Fig. 3(b)) are nearly identical, both showing $2:1$ and $3:1$ stimulation failure followed by chaos as T decreases. These results show that the APD-restitution map model (Eq. (2)) is sufficient in capturing the global APD dynamics of the AP model.

In the presence of I_{to}, we have shown that the S1S2 APD restitution curves change under different S1 pacing periods. As in the case without I_{to}, we compare the bifurcation diagrams generated by the APD-restitution map model (Eq. (2)) to the one obtained from the AP model. Fig. 4 demonstrates the APD dynamics in the case where $g_{to} = 0.278$ mS/cm² and the steady-state curve of $y_{to,f}$ is shifted by 8 mV to more negative voltages. The choice of g_{to} and the modification of $y_{to,f}$ provide an example where stimulation failure does not occur.

In the presence of I_{to}, complex APD dynamics, including alternans and chaos, occur at slower pacing periods (Fig. 4). The bifurcation diagram of the AP model, seen in Fig. 4(b), shows instability occurring in the range 536 ms $\leq T \leq 1183$ ms, and in addition there is a window of chaos for pacing periods between 536 ms and 639 ms. The bifurcation diagrams generated from the APD-restitution map model (Eq. (2)) using restitution curves with $T_{S1S1} = 400$ ms (Fig. 4(c)) and $T_{S1S1} = 2000$ ms (Fig. 4(d)) each reveals a window of instability that is significantly smaller than the window of instability of the AP model. In the $T_{S1S1} = 400$ ms case, instability occurs in the range 534 ms $\leq T \leq 897$ ms, and in the $T_{S1S1} = 2000$ ms case, the instability range is 820 ms $\leq T \leq 1196$ ms. Besides the narrow range of instability, the APD-restitution map model (Eq. (2)) does not have a chaotic region near the left-most bifurcation
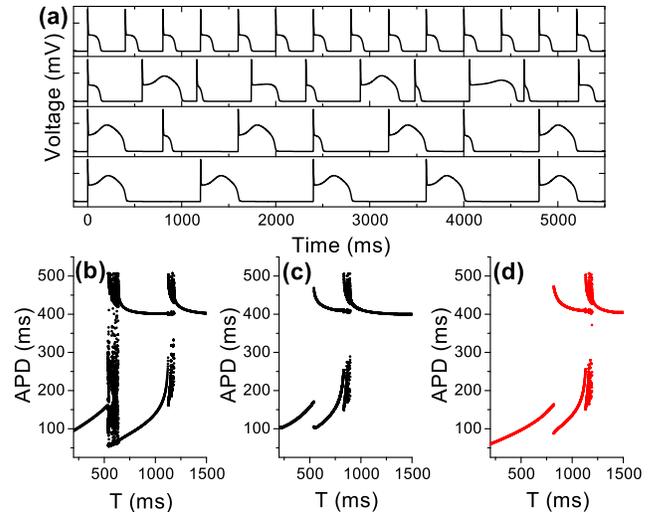

FIG. 4. APD dynamics of the LR1 model in the presence of I_{to}, with $g_{to} = 0.278$ mS/cm² and the $y-$gate shifted by 8 mV to more negative voltages. **(a)**. Sample APs from the model when the pacing period is (from top to bottom) $T = 400$ ms (stable APs with spikes), 580 ms (chaos), 800 ms (alternans), and 1200 ms (stable APs with spike-and-domes). **(b)**. Bifurcation diagram of the AP model. **(c)**. Bifurcation diagram generated from Eq. (2) using the S1S2 restitution curve with $T_{S1S1} = 400$ ms, shown in Fig. 2(d). **(d)**. Bifurcation diagram generated from the APD-restitution map model (Eq. (2)) using the S1S2 restitution curve with $T_{S1S1} = 2000$ ms, also shown in Fig. 2(d).

point as revealed in the AP model. This demonstrates that the APD-restitution map model (Eq. (2)), without incorporating memory, cannot correctly capture the dynamics of the AP model.

To show how I_{to} affects the APD dynamics, we change the intensity of I_{to} by changing its maximum conductance g_{to} and plot a contour map that reveals the APD dynamics of the model for different pacing periods. Fig. 5 shows the results, demonstrating how increasing the intensity of I_{to} increases and shifts the region of instability towards longer pacing periods. Increased levels of g_{to} cause instability to occur for longer pacing periods until g_{to} reaches a threshold. In this particular example, when $g_{to} = 0.284$ mS/cm² alternans occurs for pacing periods up to $T = 2000$ ms, equivalent to 30 beats/min. When g_{to} is larger, the AP becomes a spike without the spike-and-dome morphology, and no instability occurs.

3. An iterated map model incorporating the memory effects

In the absence of I_{to} the APD-restitution map model (Eq. (2)) can well capture the overall APD dynamics, as demonstrated in Fig. 3. However, in the presence of I_{to}, the iterated map model fails to appropriately capture
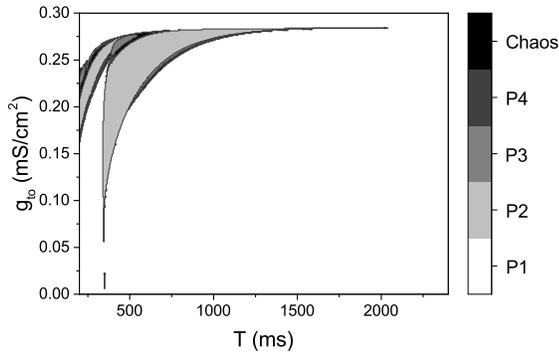
FIG. 5. Contour plot of the excitation dynamics of the AP model as a function of g_{to}, the maximal conductance of I_{to}, and the pacing period T. P1 = period-1, P2 = period-2 (alternans), P3 = period-3, P4 = period-4.

FIG. 6. Behavior of the $X-$gating variable. **(a)**. Voltage dependence of the time constant τ_X. **(b)**. Voltage dependence of the steady state X_∞. **(c)**. Sample plot of X (dashed/red) alongside APs (solid/black) undergoing alternans. X increases during the APs and decreases during the DIs, and a larger value of X precedes a spike (short APD, a_n) while the smaller value of X precedes a spike-and-dome (long APD, a_{n+1}).

the APD dynamics due to a significant effect of memory. To reveal the effects of memory on APD dynamics, we develop a new iterated map model that explicitly incorporates memory. As discussed previously, the source of memory in the LR1 model is from the slow recovery of I_K due to the slow activation and deactivation kinetics of the $X-$gating variable, where $I_K = \overline{G_K} \cdot X \cdot X_i \cdot (V - E_K)$ [55]. The kinetics of X are described by the following differential equation [55]:

$$\frac{dX}{dt} = \frac{X_\infty - X}{\tau_X}, \qquad (8)$$

where $X_\infty \equiv X_\infty(V)$ is the voltage-dependent steady-state of X, and $\tau_X \equiv \tau_X(V)$ is the voltage-dependent time constant of X. The dependence of X_∞ and τ_X on voltage is given in the LR1 model, and is shown in Fig. 6(a)-(b). Importantly, the τ_X curve shows that the time constant is about $200\,\mathrm{ms}$ at resting membrane potentials of around $-85\,\mathrm{mV}$ and peaks at around $600\,\mathrm{ms}$, when the cell is depolarized. All other gating variables in the model have very fast time constants less than $100\,\mathrm{ms}$ for all voltages, and thus cannot contribute to the source of memory.

Fig. 6(c) provides an example showing the relation between X and voltage of a cell undergoing alternans. X increases during the AP, and then decreases during the DI. In the example given, a_n and a_{n+1} are corresponding APDs of short and long APDs, respectively. The value of X preceding the short AP (x_n) is larger compared to X preceding the long AP (x_{n+1}). In other words, a larger initial X value gives rise to a shorter AP and vice versa. Physiologically, this corresponds to a larger repolarization force [60] due to a higher open probability of the K^+ channels, giving rise to early repolarization. Note that the maximum X value is much smaller during the short AP than during the long AP.

Since the $X-$gating variable is responsible for the memory in the LR1 model, we develop an iterated map
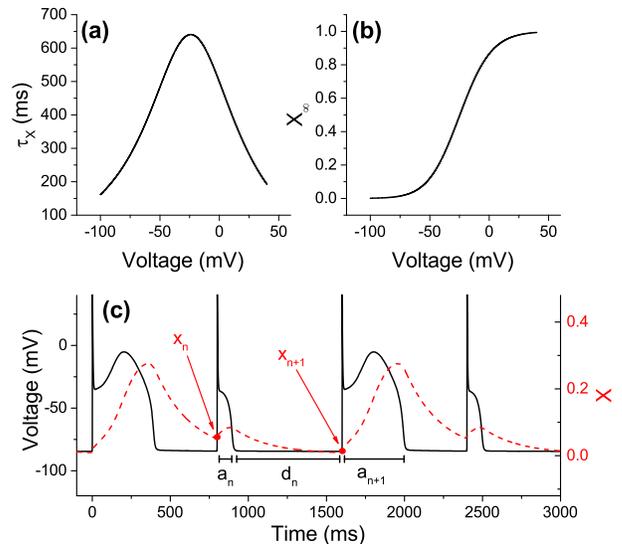
equation describing the relation between x_n and x_{n+1}, and the relation between a_n and x_n. To develop the iterated map equation for x_n, we approximate the AP to be a square wave in which the cell has a constant voltage V_a during the AP and a constant voltage V_d during its diastolic phase. See Fig. 7(a) for a visualization of the square wave approximation of an AP. Under this approximation, $\tau_a \equiv \tau_X(V_a)$ is the time constant of X during the AP, and $\tau_d \equiv \tau_X(V_d)$ is the time constant during the DI. Similarly, $x_a \equiv X_\infty(V_a)$ is the steady state open probability during the AP, and $x_d \equiv X_\infty(V_d)$ is the steady state open probability during the DI.

Let x_n be the value of X at the beginning of an AP with APD a_n and DI d_n (as shown in Fig. 6(c)). Assuming the square wave approximation with the time constants and steady state values given, Eq. (8) can be integrated exactly. Assuming that at equilibrium X is completely deactivated during the resting potential, so that $x_d \equiv 0$, this gives rise to the following map:

$$x_{n+1} = \left(x_a - (x_a - x_n)e^{-\frac{a_n}{\tau_a}}\right)e^{-\frac{d_n}{\tau_d}} \equiv w(x_n, a_n, d_n). \qquad (9)$$

Eq. (9) provides an iterated map for X from beat to beat, assuming the APD and DI values a_n and d_n are provided as well. We assume that a_n is completely determined by x_n, i.e.,

$$a_n = g(x_n), \qquad (10)$$
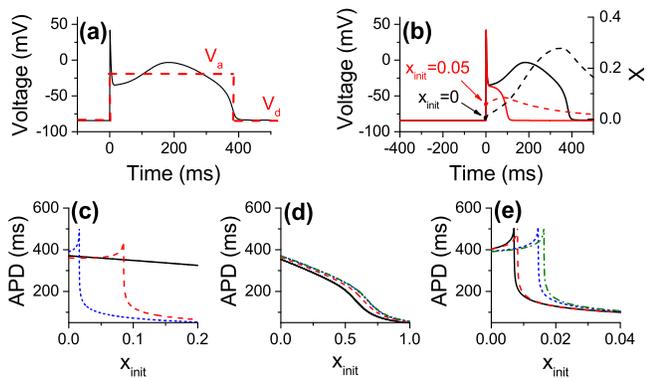
where g provides the APD-dependence on the memory

FIG. 7. Effects of the $X-$gating variable on APD. **(a)**. Square wave approximation of an AP used for the derivation of the map in Eq. (9). The resting membrane potential is V_d and the depolarized membrane potential is V_a. **(b)**. The dependence of APD on the initial value of X, x_{init}. When $x_{init} = 0$ the resulting AP exhibits a spike-and-dome, whereas when $x_{init} = 0.05$ the resulting AP is a spike. The AP with a longer APD (spike-and-dome) causes X to increase for a longer period of time. **(c)**. APD dependence curves on x_{init} for different maximal conductance levels $g_{to} = 0\,\mathrm{mS/cm^2}$ (solid/black), $0.24\,\mathrm{mS/cm^2}$ (dashed/red), $0.278\,\mathrm{mS/cm^2}$ (short-dashed/blue). **(d)**. Without I_{to} ($g_{to} = 0\,\mathrm{mS/cm^2}$) APD dependence curves on X for different diastolic intervals preceding the AP, DI = $50\,\mathrm{ms}$ (solid/black), $100\,\mathrm{ms}$ (dashed/red), $200\,\mathrm{ms}$ (short-dashed/blue), $1000\,\mathrm{ms}$ (dash-dotted/green). **(e)**. Same as (d), but with I_{to} ($g_{to} = 0.278\,\mathrm{mS/cm^2}$).

variable x_n. And since the pacing period T satisfies the equation $mT = a_n + d_n$, then

$$d_n = mT - a_n, \qquad (11)$$

where m is the number of stimuli before giving a new beat.

Together, Eqs. (9)-(11) form a complete 1-dimensional iterated map. We next determine the function g in Eq. (10), which captures the dependence of APD on the value of X at the beginning of the AP, x_{init}. In a similar fashion to the S1S2 restitution protocol which serves to find the dependence of APD on DI, here we use another simulation protocol to determine the dependence of APD on x_{init}. At a fixed pacing period, e.g. $T = 1000\,\mathrm{ms}$, after a certain number of N pre-paced beats we change the value of x_{init} at the time of the $(N+1)^{st}$ stimulus and record the resulting APD. Fig. 7(b) provides examples of APs when $x_{init} = 0$ and $x_{init} = 0.05$, in which 100 pre-paced beats were used. $x_{init} = 0$ results in an AP with a spike-and-dome and an APD of about $400\,\mathrm{ms}$, whereas when $x_{init} = 0.05$ the resulting AP is a spike with a shortened APD of about $100\,\mathrm{ms}$.

I_{to} causes shifts in the APD-dependence curves on x_{init}, as demonstrated in Fig. 7. Without I_{to} ($g_{to} = 0\,\mathrm{mS/cm^2}$) the APD has a maximum at $375\,\mathrm{ms}$ when $x_{init} = 0$ and smoothly decreases as x_{init} increases. When I_{to} is included, there appears a critical x_{init} value

in which APD sharply declines from over $300\,\mathrm{ms}$ to less than $100\,\mathrm{ms}$, indicating a sensitive dependence of APD on x_{init}. For values less than the critical x_{init} value, the APD is temporarily increasing as a function of x_{init}, but is then decreasing beyond the critical value. In Fig.7(c), the dashed/red and short-dashed/blue curves show the APD dependence on x_{init} for $g_{to} = 0.24\,\mathrm{mS/cm^2}$ and $g_{to} = 0.278\,\mathrm{mS/cm^2}$. When the conductance of I_{to} is weaker (dashed/red curve), the critical value occurs around $x_{init} = 0.08$, while when the conductance is stronger (short-dashed/blue curve), the critical value occurs around $x_{init} = 0.02$. In general, the critical x_{init} value shifts to the left as g_{to} increases, due to a change in the balance of $I_{to}-$induced early repolarization.

We next test how accurately x_{init} alone affects APD. To do so, we check the APD dependence on x_{init} when the DI itself varies as well. Fig. 7(d)-(e) each shows four different curves for different values of DI, $50\,\mathrm{ms}$, $100\,\mathrm{ms}$, $200\,\mathrm{ms}$, and $1000\,\mathrm{ms}$, without and with I_{to}. In both cases, the curves shift to the left for decreasing values of DI, but is more pronounced when DI = $50\,\mathrm{ms}$ and $100\,\mathrm{ms}$. The curves corresponding to DI = $200\,\mathrm{ms}$ and DI = $1000\,\mathrm{ms}$ vary by only about 0.002. Therefore, this indicates that the recovery of other ionic currents visibly affects the APD only when DI < $100\,\mathrm{ms}$. As shown in Fig. 4, dynamical instabilities occur for DI $\gg 100\,\mathrm{ms}$, indicating that recovery of I_K plays the major role in causing instability in the presence of I_{to}. This also justifies not incorporating DI as an explicit variable in the iterated map model in Eq. (12). For the same reason, in this study, we ignore the APD dynamics at very fast pacing and plot our bifurcation diagrams for $T > 200\,\mathrm{ms}$ (except for Figs. 3 and 16). In general, one can rewrite Eq. (12) as $a_n = g(x_n, d_n)$ to include contributions from the recovery of other ionic currents, which could be important for APD dynamics at fast heart rates.

4. Memory-induced instabilities and complex APD dynamics in the $X-$memory map model

The $X-$memory map model (Eqs. (9)-(11)) explicitly incorporates memory and its coupling with APD, in contrast to the APD-restitution map model using the S1S2 restitution curve as in Eq. (2). As shown in Fig. 4, when I_{to} is included, the APD-restitution map model (Eq. (2)) does not adequately capture the APD dynamics in the AP model. We here show that the $X-$memory map model (Eqs. (9)-(11)) does in fact accurately capture the APD dynamics and bifurcations of the AP model.

We first use the same model parameters and modifications that were used to generate Fig. 4, in which $g_{to} = 0.278\,\mathrm{mS/cm^2}$ and the $y_{to}-$gate steady state in the formulation for I_{to} was shifted by $8\,\mathrm{mV}$ to more negative voltages. Under the square-wave assumption used to generate Eq. (9), we set the map parameters $x_a = 0.6, \tau_a = 600\,\mathrm{ms}$, and $\tau_d = 200\,\mathrm{ms}$. Computationally, we determine the APD dependence on X, the
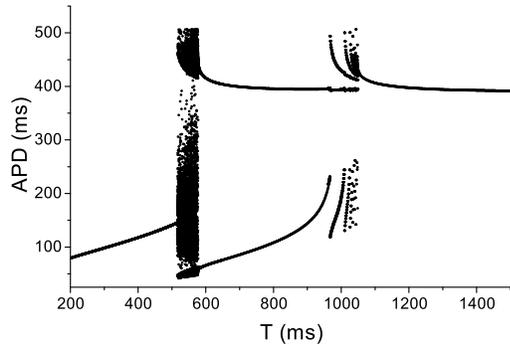
FIG. 8. Bifurcation diagram of the APD dynamics captured by the $X-$memory map model, Eqs. (9)-(11), with $x_a = 0.6, \tau_a = 600\,\text{ms}, \tau_d = 200\,\text{ms}$, and g provided by interpolating the short-dashed/blue curve in Fig. 7(c).

FIG. 9. Complex APD dynamics captured by the $X-$memory map model (Eqs. (13)-(15)), with the following parameter modifications of the AP model: $g_{to} = 0.21\,\text{mS/cm}^2, G_{si} = 0.1035\,\text{mS/cm}^2, G_{K1} = 1.330\,34\,\text{mS/cm}^2, \tau_x \to 5\tau_x$, and the y_{to} steady state curve shifted by $8\,\text{mV}$ to more positive voltages. **(a)**. S1S2 restitution curves of the AP model with S1 pacing periods $T_{S1S1} = 300\,\text{ms}$ (solid/black) and $1000\,\text{ms}$ (dashed/red). **(b)**. APD dependence on X. **(c)**. Bifurcation diagram of the APD-restitution map model (Eq. (2)) using the solid/black curve in (a). **(d)**. Bifurcation diagram of the APD-restitution map model (Eq. (2)) using the dashed/red curve in (a). **(e)**. Bifurcation diagram of the AP model. **(f)**. Bifurcation diagram of the $X-$memory map model (Eqs. (9)-(11)), with $x_a = 0.6, \tau_a = 3000\,\text{ms}, \tau_d = 1000\,\text{ms}$, and g provided by interpolating the curve in (b).

function g in Eq. (10). By varying the cycle length T in Eq. (11) we generate a bifurcation diagram by iterating together Eqs. (9)-(11).

The resulting bifurcation diagram is shown in Fig. 8. The diagram is very similar in topology to the bifurcation diagram obtained directly from the AP model, as seen in Fig. 4(b). In particular, both diagrams have windows of chaos near the initial period-doubling bifurcation point near $T = 500\,\text{ms}$, which was completely absent in the bifurcation diagrams generated from the APD-restitution map model, as in Fig. 4(c)-(d).

The APD dependence on x_{init} shown in Fig. 7(c) is nonmonotonic, in which as x_{init} increases, the value of APD increases until around $x_{init} = 0.02$ when the curve suddenly drops to APD values less than $150\,\text{ms}$. Similarly, the S1S2 restitution curves are nonmonotonic. As shown previously, a nonmonotonic APD restitution curve can give rise to chaos [22], as is shown in Fig. 4(c)-(d). To avoid the confluent effect of nonmonotonicity on the genesis of chaos, we changed the parameters of the LR1 model to result in monotonic APD restitution curves, which is shown in the next example below.

The parameter changes are the following: $g_{to} = 0.21\,\text{mS/cm}^2, G_{si} = 0.1035\,\text{mS/cm}^2, G_{K1} = 1.330\,34\,\text{mS/cm}^2$, and $\tau_x \to 5\tau_x$. In addition, the y_{to} steady state curve was shifted by $8\,\text{mV}$ to more positive voltages (in the prior case, the curve was shifted to more negative voltages). Note that setting $\tau_X \to 5\tau_X$, so that the voltage-dependent time constant of the $X-$gating variable was increased 5-fold, effectively amplifies the effect of memory by requiring 5 times the amount of time for X to reach equilibrium.

The results under these different parameter changes and modifications are shown in Fig. 9. Figs. 9(a)-(b) show that indeed the restitution curves and the APD dependence on x_{init} are now monotonic. Because each restitution curve is monotonic, the APD-restitution map in Eq. (2) would only give rise to alternans (Fig. 9(c)-(d)). However, as seen in Fig. 9(e), the bifurcation diagram of
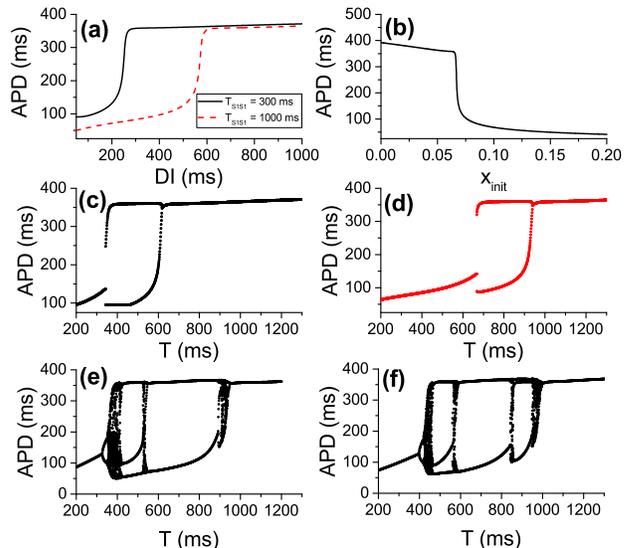
the AP model shows very complex behavior, including very clear period-doubling bifurcation routes to enter and exit chaos.

Since we made the modification $\tau_X \to 5\tau_X$, we also appropriately change the iterated map values τ_a and τ_d in the $X-$memory map model. Since $\tau_a = 600\,\text{ms}$ and $\tau_d = 200\,\text{ms}$ in the original case, here we multiply these values $5-$fold so that $\tau_a = 3000\,\text{ms}$ and $\tau_d = 1000\,\text{ms}$. $x_a = 0.6$ as before. The dynamics of the $X-$memory map model is shown in the bifurcation diagram in Fig. 9(f). The behavior of the $X-$memory map model matches very closely with the behavior of the AP model, as the bifurcation diagram also reveals period-doubling bifurcation routes to enter and exit chaos, and share other characteristics including large period-2 (alternans) and period-3 windows.

The $X-$memory map model accurately matches the dynamics of the AP model, even under crudely approximating an AP as a square wave. In contrast, the APD-restitution map in Eq. (2) does not capture the complex behavior and underestimates the regions of instability. This demonstrates that the effects of memory produce more complex behaviors.

5. Theoretical analysis and predictions of the $X-$memory map model

The $X-$memory map model (Eqs. (9)-(11)) has model parameters $x_a, \tau_a, \tau_d,$ and g, the APD dependence on curve. We assume here that g takes on the form of a Hill function, so that

$$a_n = g(x_n) = a_{min} + \frac{a_{max} - a_{min}}{1 + \left(\frac{x_n}{k_x}\right)^h}, \qquad (12)$$

where a_{min} and a_{max} are the minimum and maximum APDs, h is the Hill coefficient, and k_x is the half-max value. A Hill function was chosen to match the sigmoid-like shapes of the APD dependence curves on X, for example in Fig. 9(b). So now, Eqs. (9), (11), and (12) form an iterated map model, written together below:

$$x_{n+1} = w(x_n, a_n, d_n) = \left(x_a - (x_a - x_n)e^{-\frac{a_n}{\tau_a}}\right)e^{-\frac{d_n}{\tau_d}}, \qquad (13)$$

$$a_n = g(x_n) = a_{min} + \frac{a_{max} - a_{min}}{1 + \left(\frac{x_n}{k_x}\right)^h}, \qquad (14)$$

$$d_n = mT - a_n. \qquad (15)$$

This produces a 1-dimensional iterated map for X since

$$x_{n+1} = w(x_n, a_n, d_n) = w(x_n, g(x_n), mT - g(x_n)) \equiv W(x_n). \qquad (16)$$

And in addition, via the function g, there is a one-to-one correspondence between x_n and a_n. In particular, the inverse of g is obtained via the following formula:

$$x_n = g^{-1}(a_n) = k_x \left[\frac{a_{max} - a_n}{a_n - a_{min}}\right]^{\frac{1}{h}}, \qquad (17)$$

so that

$$a_{n+1} = g(x_{n+1}) = g(W(x_n)) = g(W(g^{-1}(a_n))) \equiv H(a_n) \qquad (18)$$

Eq. (18) is the APD return map for the $X-$memory map model. Sample return maps are provided in Fig. 10 when varying the Hill parameter h, the pacing period T, and the time constant τ_d. When varying h (Fig. 10(a)), the slope of the return map near the fixed point gets steeper as h increases. An iterated map is unstable when the slope (or derivative) at the fixed point has absolute value exceeding unity, and thus h is a key factor in determining stability. In addition, as seen in Fig. 10(b)-(c), increasing T or decreasing τ_d tends to shift the return map to the right, and therefore shifting the fixed point. Fig. 10(d) shows a return map from a chaotic region in the actual AP model. Note that the Hill function is monotonic and so is the S1S2 APD restitution curve. For a nonmonotonic APD restitution function, the first return map from Eq. (2) is still nonmonotonic. However,
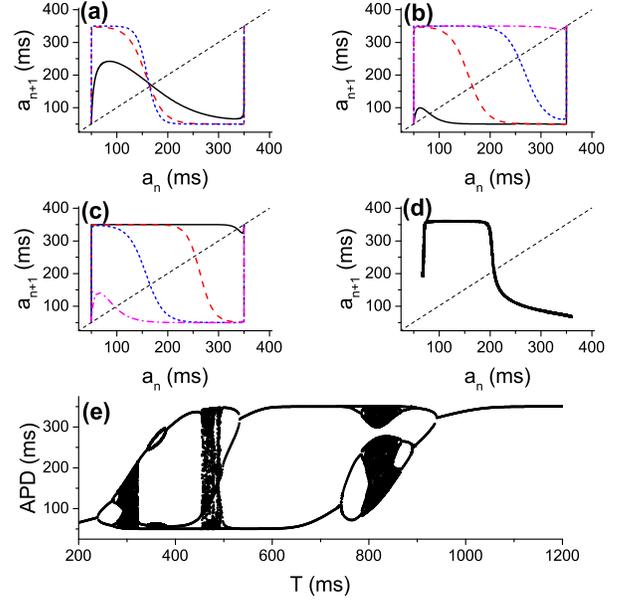

FIG. 10. Return maps of the $X-$memory map model (Eqs. (13)-(15)) and of the AP model. Default parameter values are $x_a = 0.6, \tau_a = 3000\,\text{ms}, \tau_d = 1000\,\text{ms}, h = 25, k_x = 0.07, T = 500\,\text{ms}, a_{min} = 50\,\text{ms}, a_{max} = 350\,\text{ms}$. **(a)**. Return maps for $h = 10$ (solid/black) 20 (dashed/red), 40 (short-dashed/blue). **(b)**. Return maps for varying $T = 250\,\text{ms}$ (solid/black), $500\,\text{ms}$ (dashed/red), $750\,\text{ms}$ (short-dashed/blue), $1000\,\text{ms}$ (dash-dotted/magenta). **(c)**. Return maps for $\tau_d = 250\,\text{ms}$ (solid/black), $500\,\text{ms}$ (dashed/red), $1000\,\text{ms}$ (short-dashed/blue), $2000\,\text{ms}$ (dash-dotted/magenta). **(d)**. Return map from the AP model as in Fig. 9(e) in a chaotic region with $T = 530\,\text{ms}$. **(e)**. Bifurcation diagram of the $X-$memory map model (Eqs. (13)-(15)), with parameter values $x_a = 0.6, \tau_a = 3000\,\text{ms}, \tau_d = 1000\,\text{ms}, h = 25, k_x = 0.07$.

the addition of the memory equation into the iterated map model results in a nonmonotonic map, agreeing with the one from simulation of the AP model. This indicates that memory plays a key role in promoting chaos by converting a monotonic APD return map to a nonmonotonic one.

Fig. 10(e) provides a sample bifurcation diagram from the $X-$memory map model, using the default map parameter values $x_a = 0.6, \tau_a = 3000\,\text{ms}, \tau_d = 1000\,\text{ms}, h = 25, k_x = 0.07, a_{min} = 50\,\text{ms}, a_{max} = 350\,\text{ms}$. Just as for the full AP model, the diagram shows period-doubling bifurcation routes to enter and exit chaos, with rather large period-2 and period-3 windows. See Fig. 9(e) to compare with the bifurcation diagram from the AP model.

We now perform a stability analysis of the fixed point of the $X-$memory map model. The APD fixed point, denoted a^*, satisfies $a^* = H(a^*)$ so that

$$a^* = H(a^*) = g\left[\left(x_a - (x_a - x^*)e^{-\frac{a^*}{\tau_a}}\right)e^{-\frac{T - a^*}{\tau_d}}\right], \qquad (19)$$

where $x^* = g^{-1}(a^*)$ is the corresponding X fixed point.

To analyze the stability of the fixed point, we find $H'(a^*)$, the derivative of H in Eq. (18) evaluated at the fixed point a^*.

$$H'(a^*) = g'(x^*)\left[\left(\frac{1}{\tau_d} - \frac{1}{\tau_a}\right)x^* + e^{-\frac{T-a^*}{\tau_d}}\left(\frac{e^{-\frac{a^*}{\tau_a}}}{g'(x^*)} + \frac{x_a}{\tau_a}\right)\right],$$
(20)

where

$$g'(x^*) = -\frac{h}{x^*}\frac{(a_{max} - a^*)(a^* - a_{min})}{a_{max} - a_{min}}.$$
(21)

The map is unstable whenever $|H'(a^*)| > 1$.

Based on Eq. (11), for $|H'(a^*)| > 1$, a large $g'(x^*)$ is needed, indicating that a sensitive response of APD on X is necessary. The presence of I_{to} results in such a steep response to promote the instability. However, the stability also depends on other parameters, such as τ_a and τ_d. Since it is not obvious from Eq. (20) to assess their roles, we simulate the $X-$memory map model directly to show their effects. Fig. 11 provides some relationships between the model parameters T, τ_d, τ_a, and h, and the overall stability of the $X-$memory map model. The periodicity of the iterated map is provided for different parameter values of T, τ_d, τ_a, and h, with white regions indicating stability (P1), and increasing gray-scale intensities indicating higher orders of periodicity (P2, P3, P4, and chaos).

Fig. 11(a) shows the APD dynamics in the parameter space of the time constant τ_d and the pacing period T, with constants $\tau_a = 3000\,\text{ms}$ and $h = 25$ fixed. There is a linear relationship between τ_d and T on stability, in which an increase in τ_d causes both an expansion and a shift to the right of the instability region for varying values of T. Fig. 11(b) shows the APD dynamics in the parameter space of h and T, with constants $\tau_a = 3000\,\text{ms}$ and $\tau_d = 1000\,\text{ms}$ fixed. As one would expect, an increase in h causes the window of instability to increase and expands the chaotic regimes until h is very large. Fig. 11(c) shows the APD dynamics in the parameter space of h and τ_d while keeping constants $\tau_a = 3000\,\text{ms}$ and $T = 500\,\text{ms}$ fixed. Again as expected, increasing h increases the regime of instability and chaos, while at the same time increasing τ_d reduces the instability region. Finally, Fig. 11(d) shows the APD dynamics in the parameter space of the time constants τ_a and τ_d while keeping constants $h = 25$ and $T = 500\,\text{ms}$ fixed. Similar to that seen in Fig. 11(a), there is at first a linear relationship between τ_a and τ_d, in which an increase in τ_a causes an increase in the instability region for various values of τ_d. However, when both τ_a and τ_d get too large, the instability region wraps around and closes.

The previous analysis using the $X-$memory map model examines the effects of different parameters on stability, in particular on the parameters τ_d and τ_a that affect the activation and inactivation kinetics of I_K. We now test our results on the AP model. Since τ_d affects only the inactivation of I_K during the DI, changing τ_d
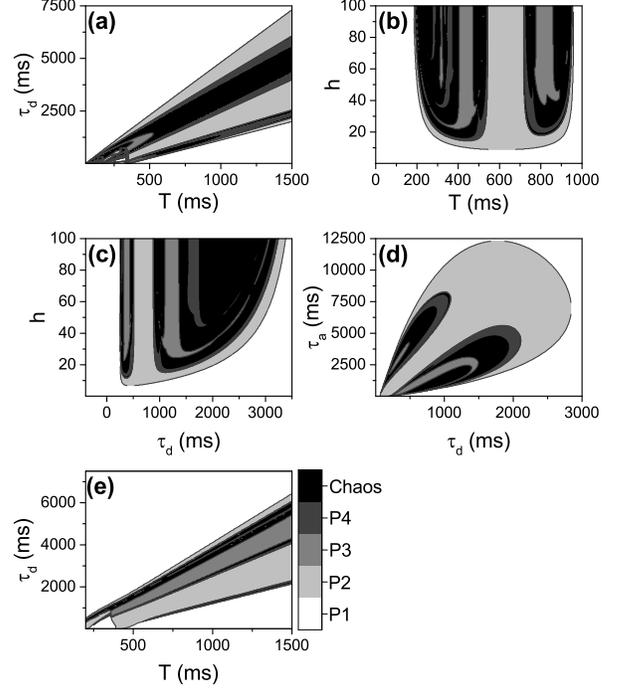

FIG. 11. Stability maps when varying parameters of the $X-$memory map model (Eqs. (13)-(15)). Default parameter values are as follows: $x_a = 0.6, \tau_a = 3000\,\text{ms}, \tau_d = 1000\,\text{ms}, h = 25, k_x = 0.07$. (a). Contour map showing stable and unstable regions when varying the time constant τ_d and pacing period T. (b). Stable and unstable regions when varying the Hill coefficient h and T. (c). Stable and unstable regions when varying h and τ_d. (d). Stable and unstable regions when varying the APD and DI time constants τ_a and τ_d. (e). Stable and unstable regions of the modified AP model using the τ_X modification in Eq. (22), with the following parameter modifications: $g_{to} = 0.21\,\text{mS/cm}^2, G_{si} = 0.1035\,\text{mS/cm}^2, G_{K1} = 1.330\,34\,\text{mS/cm}^2, \tau_x \to 5\tau_x$, and the y_{to} steady state curved shifted by $8\,\text{mV}$ to more positive voltages.

will ideally have little effect on AP morphology (in contrast to changing τ_a). We change the model formulation of τ_X to equal a set value τ_d during the DI, as follows:

$$\tau_X = \begin{cases} \tau_d & V < -75\,\text{mV} \\ \overline{\tau_X} & \text{otherwise} \end{cases}.$$
(22)

$\overline{\tau_X}$ is the original formulation of τ_X in the AP model, for example that shown in Fig. 6(a). τ_d is now a new parameter in the AP model, and as before we vary τ_d as well as the pacing period T for stability analysis. Fig. 11(e) shows the results using the AP model with the same parameter and formulation modifications to generate Fig. 9, including $\overline{\tau_X} \to 5\overline{\tau_X}$. The figure shows a clear resemblance to Fig. 11(a), showing that increasing τ_d results in a shift and expansion of the region of instability. The theoretical prediction matches closely with the simulation results.
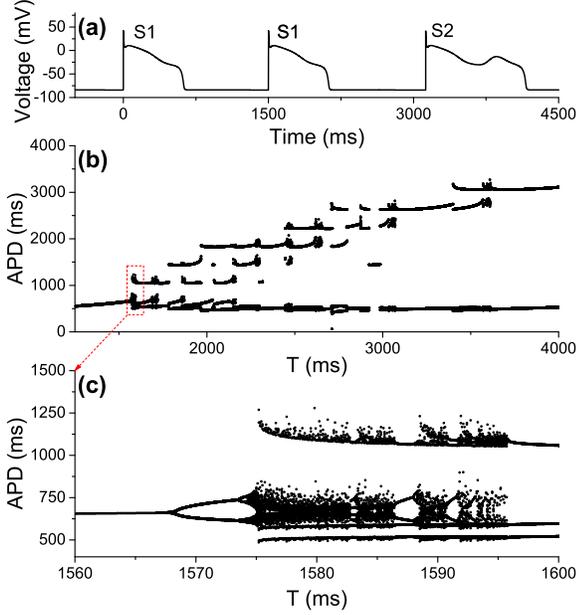
FIG. 12. EAD and APD dynamics in the LR1 model with $\tau_X \to 10\tau_X$ and without I_{to} included. All other parameter values are taken from the original model formulation. **(a)**. An S1S2 protocol resulting in an EAD on the S2 beat, with $T_{S1S1} = 1500$ ms, and DI = 1000 ms before the S2 beat. **(b)**. Bifurcation diagram of the AP model. **(c)**. Close up of the bifurcation diagram around the first bifurcation point.

6. The memory effects on EAD-induced complex APD dynamics

Short-term memory is also nontrivial for the excitation dynamics in the setting of long QT syndrome. Long QT syndrome is a cardiac disease with a high risk of syncope and sudden death, caused by genetic mutations or drugs that either decrease outward currents or increase inward currents, prolonging the APD [51, 61]. One of the consequences of APD prolongation is the occurrence of EADs (Fig. 12(a)), which are abnormal depolarizations during the AP. In previous studies [13, 62, 63], we have shown that the presence of EADs can lead to chaotic excitation dynamics. Fig. 12(b) is a bifurcation diagram against the pacing period T from a simulation of the LR1 model, showing a period-doubling bifurcation leading to complex excitation patterns and chaos. Fig. 12(c) is a higher resolution bifurcation diagram around the first bifurcation point, demonstrating with more detail the period doubling leading to chaos. The underlying mechanism of chaos was attributed to steep and nonmonotonic APD restitution functions [13]. However, a detailed comparison between the bifurcation from the AP model and that from the iterated map model has not been carried out until our recent study which showed that memory plays a key role [38].

Following the same pacing protocol as we have done for the case of I_{to} (there is no I_{to} presence in this case), we
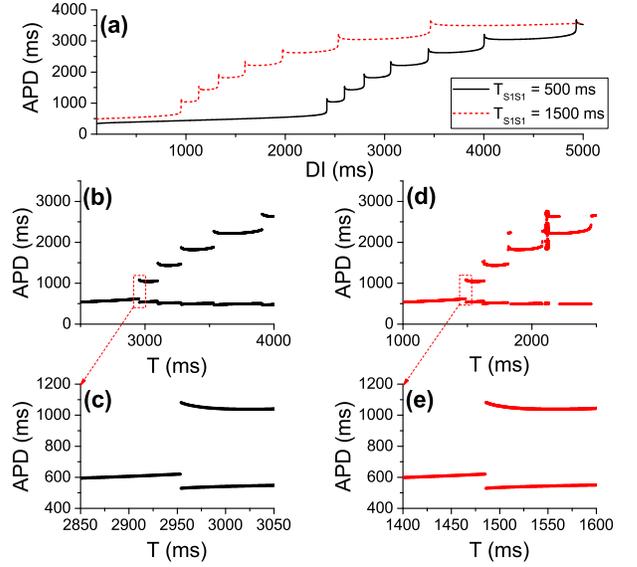

FIG. 13. EAD dynamics predicted by S1S2 APD restitution curves. **(a)**. S1S2 restitution curves for two S1 pacing periods $T_{S1S1} = 500$ ms (solid/black) and 1500 ms (dashed/red). **(b)**. Bifurcation diagram using the APD-restitution map model (Eq. (2)) and the restitution curve with S1 pacing period $T_{S1S1} = 500$ ms (solid/black curve in (a)). **(c)**. Close up of the bifurcation diagram around the first bifurcation point. **(d)**. Bifurcation diagram using the APD-restitution map model (Eq. (2)) and the restitution curve with S1 pacing period $T_{S1S1} = 1500$ ms (dashed/red curve in (a)). Close up of the bifurcation diagram around the first bifurcation point.

calculate the S1S2 APD restitution curves for two different S1 pacing periods (Fig. 13(a)). The S1S2 APD restitution curves exhibit a staircase type increase against DI, with each higher step corresponding to an extra EAD in the AP. Faster S1 pacing causes the APD restitution curve to shift to the right (note that this is in contrast to the case in the presence of I_{to}, in which the APD restitution curve shifts to the left under faster S1 pacing, as shown in Fig. 2(f) and Fig. 9(a). Fig. 13(b) and (d) show the bifurcation diagrams obtained using the APD-restitution map model (Eq. (2)) and the S1S2 APD restitution curves. However, higher resolution bifurcation diagrams around the onset of instability (Figs. 13(c) and (e)) show sudden transitions for stable APD to APD alternans, completely missing the supercritical period doubling bifurcation sequences of the AP model.

We then use the same method as in the case with I_{to} and measure the $X-$dependence curve of APD. Fig. 14(a) shows a staircase dependence of APD on x_{init}. Using the $X-$memory map model (Eqs. (9)-(11)) with the $X-$dependence curve of APD in Fig. 14(a), we generate a new bifurcation diagram (Fig. 14(b)), which shows almost exactly the same bifurcation sequence as in the AP model. Fig. 14(c) shows the bifurcation sequence around the first instability point, which clearly demonstrates period doubling leading to chaos in a very simi-
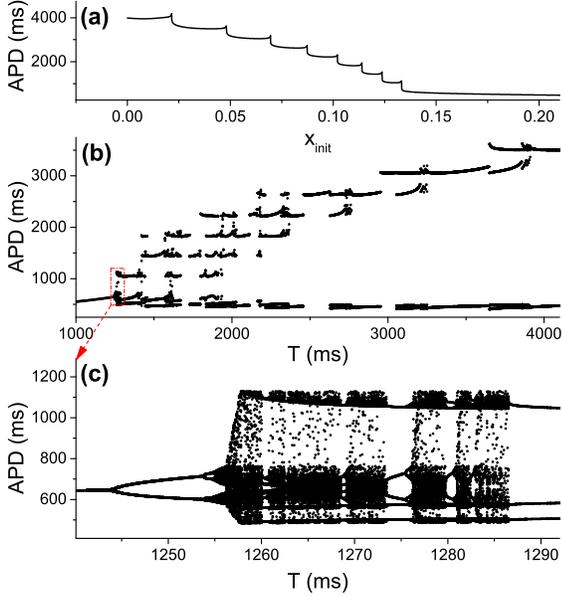
FIG. 14. Bifurcation diagrams from the $X-$memory map model (Eqs. (9)-(11)) in the presence of EADs. **(a)**. The dependence of APD on x_{init}. **(b)**. Bifurcation of the $X-$memory map model (Eqs. (9)-(11)), using the curve in panel (a) for g and model parameters $x_a = 0.6$, $\tau_a = 6000$ ms, and $\tau_d = 2500$ ms. **(c)**. Close-up of the bifurcation diagram in (b) around the first bifurcation point.

lar manner as in the AP model (compare to Fig. 12(c)). These results indicate that memory plays an important role in generating the complex EAD-related excitation dynamics.

B. Complex APD dynamics caused by memory originating from intracellular ion concentration accumulation

Besides slow recovery of ion channels, it also takes a certain amount of time for intracellular ion (Na^+, K^+, and Ca^{2+}) concentrations to reach new steady states after a change, such as after a sudden change in the heart rate [64], causing memory in the system. Here, we demonstrate the effects of memory caused by slow $[Ca^{2+}]_i$ accumulation. We use a human ventricular cell model developed by ten Tusscher *et al.* [56], the TP04 model, to investigate the effects of memory originating from intracellular ion concentration accumulation. For consistency, we remove the original I_{to} (both fast and slow I_{to}) and replace them with the same I_{to} formulation as before from Mahajan *et al.* [57].

We use the TP04 model because all ionic gating variables have relatively fast time constants during the diastolic phase. In particular, the two slowly activating potassium currents, I_{Kr} and I_{Ks}, rapidly deactivate during the diastolic phase. The two gating variables of

I_{Kr}, X_{r1} and X_{r2}, and the gating variable of I_{Ks}, X_s, have time constants $\tau_{x_{r1}} < 130$ ms, $\tau_{x_{r2}} < 2$ ms, and $\tau_{x_s} < 5$ ms at voltages lower than -75 ms. And so, while the gating variables of these currents do have long time constants as high as 1200 ms in the model for voltages higher than -40 mV, the gating variables deactivate rapidly during the diastolic interval. In contrast, $[Ca^{2+}]_i$ as well as intracellular Na^+ and K^+ concentrations ($[Na^+]_i$ and $[K^+]_i$) accumulate very slowly.

Since $[Na^+]_i$ and $[K^+]_i$ accumulation is much slower than $[Ca^{2+}]_i$ accumulation, to avoid any confluent effects we fixed the concentrations $[Na^+]_i = 12$ mM and $[K^+]_i = 138$ mM in the TP04 model so that the memory effect is primarily driven by the accumulation of $[Ca^{2+}]_i$.

1. Memory and complex APD dynamics caused by ion concentration accumulation

We begin our analysis as before, by examining the APD restitution curves of the TP04 model with and without I_{to} and comparing the bifurcation diagrams of the APD-restitution map model (Eq. (2)) using the restitution curves with those of the AP model.

Fig. 15 shows the APD restitution curves of the AP model with and without I_{to}, in each case using two different pacing periods. Without I_{to} (Fig. 15(a)), the restitution curves using S1 pacing periods $T_{S1S1} = 750$ ms and $T_{S1S1} = 3000$ ms are both monotonically increasing, similar to the restitution curves generated from the LR1 model without I_{to} (Fig. 1(b)). There is an upward shift in the curves by about 5 ms for the larger S1 pacing period ($T_{S1S1} = 3000$ ms), indicative of some underlying source of memory in the TP04 model but that has minimal effect on restitution.

In the presence of I_{to}, with maximum conductance $g_{to} = 0.18$ mS/cm^2, the APD restitution curves show some similarity to the restitution curves generated from the LR1 model in the presence of I_{to} (Fig. 2(d)), namely that they are nonmonotonic, have steep regions with a sensitive dependence of APD on DI, and the larger S1 pacing period shifts the restitution curve to the right. Here however, the shift in the two curves is substantial, in which an S1 pacing period of $T_{S1S1} = 9000$ ms leads to a restitution curve that is about 6000 ms right-shifted from the restitution curve using an S1 pacing period of $T_{S1S1} = 250$ ms. Note that using an S1 pacing period as large as $T_{S1S1} = 9000$ ms is necessary in order to avoid instability in the APs of the pre-paced beats.

Fig. 16(a) shows the bifurcation diagram of the AP model in the absence of I_{to}. For almost all pacing periods the AP model shows stability, except for a brief region around $T = 275$ ms showing chaotic APD dynamics where there is a transition between 1:1 and 2:1 block. There is also a transition between 2:1 block and 3:1 block around $T = 125$ ms.

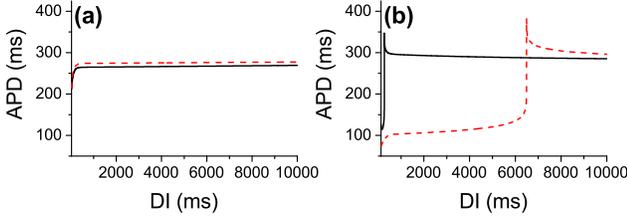Now, we examine the stability of the APD-restitution map model (Eq. (2)) using the APD restitutions in

FIG. 15. APD restitution curves of the modified TP04 model without and with I_{to}. **(a)**. APD restitution curves in the absence of I_{to}, for S1 pacing periods $T_{S1S1} = 750$ ms (solid/black) and $T_{S1S1} = 3000$ ms (dashed/red). **(b)**. APD restitution curves in the presence of I_{to} with $g_{to} = 0.18$ mS/cm^2, for S1 pacing periods $T_{S1S1} = 250$ ms (solid/black) and $T_{S1S1} = 9000$ ms (dashed/red).
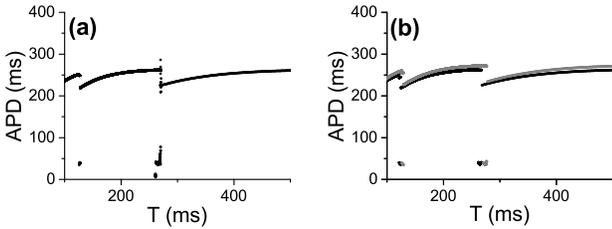

FIG. 16. Bifurcation diagrams of the AP model and of the APD-restitution map model (Eq. (2)), without I_{to}. **(a)**. Bifurcation diagram of the AP model without I_{to}. **(b)**. Bifurcation diagrams of the APD-restitution map model (Eq. (2)) using the APD restitution curves in Fig. 15(a), with $T_{S1S1} = 750$ ms (black) and $T_{S1S1} = 3000$ ms (gray).

Fig. 15. Using the APD restitutions generated from the AP model without I_{to}, the resulting bifurcation diagrams are shown in Fig. 16(b). Two bifurcation curves are generated using the two APD restitution protocols for the S1 pacing periods $T_{S1S1} = 750$ ms (black) and $T_{S1S1} = 3000$ ms (gray). The gray points are shifted upward from the black points due to the slight upward shift seen in the APD restitution curves as in Fig. 15(a). For the most part the two diagrams show stability with very small instability occurring at the transitions between 1:1 and 2:1 block and between 2:1 block and 3:1 block. Overall, the two diagrams show very similar characteristics with the bifurcation diagram of the AP model.

We now examine what happens in the presence of I_{to}. The bifurcation diagram of the AP model is shown in Fig. 17(a). Vastly different from the bifurcation diagram of the model without I_{to}, there is a large instability window with several chaotic windows, interspersed with periodic windows. The first period-doubling bifurcation point occurs around $T = 330$ ms, and for even very slow pacing periods up to $T = 9000$ ms there is still APD alternans and higher periodicity including chaos.

Using the APD-restitution map model (Eq. (2)), we develop bifurcation diagrams generated from the APD restitution curves in Fig. 15(b) with different S1 pac-
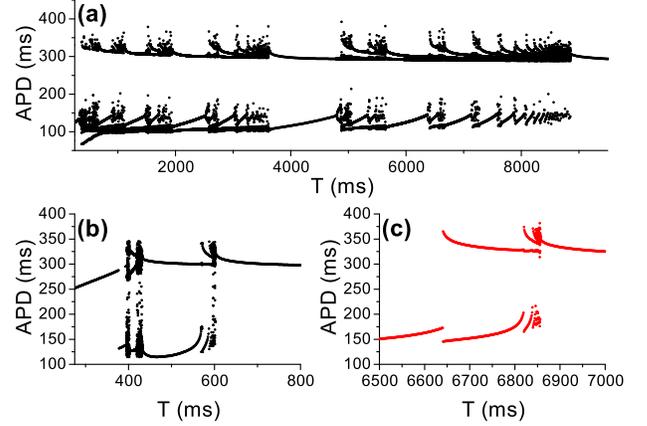

FIG. 17. Bifurcation diagrams of the AP model and of the APD-restitution map model (Eq. (2)), in the presence of I_{to} with maximum conductance $g_{to} = 0.18$ mS/cm^2. **(a)**. Bifurcation diagram of the AP model. **(b)**. Bifurcation diagram of the APD-restitution map model using the solid/black trace ($T_{S1S1} = 250$ ms) in the APD restitution curves in Fig. 15(b). **(c)**. Bifurcation diagram of the APD-restitution map model using the dashed/red trace ($T_{S1S1} = 9000$ ms) in Fig. 15(b).

ing periods. The rightward shift in restitution by about 6000 ms produces two bifurcation curves with very different regions of APD instability, as seen in Figs. 17(b)-(c). With the restitution curve generated from an S1 pacing period $T_{S1S1} = 250$ ms, the range of instability occurs between pacing periods $T = 400$ ms and 600 ms, while with the restitution curve generated from an S1 pacing period $T_{S1S1} = 9000$ ms, the range of instability is between $T = 6650$ ms and 6850 ms. The regions of chaos and instability with periods greater than 2 are due to the nonmonotonicity of the APD restitution curves, just as in the case with the LR1 model in the presence of I_{to} (see Fig. 4(c)-(d)).

The bifurcation diagrams generated from the APD-restitution map model (Eq. (2)) in the presence of I_{to} reveal windows of instability about 200 ms in length. However, the bifurcation diagram of the AP model reveals an instability window that is much greater, with several chaotic windows. It is clear in this case that the APD-restitution model in Eq. (2) does not at all predict the APD dynamics of the AP model. The memory in the TP04 model driven by the slow accumulation of $[\text{Ca}^{2+}]_i$ produces massive effects on the AP model dynamics, leading to a much greater window of instability and chaos.

2. An iterated map model incorporating the memory effects

In the previous section, we discussed the role of the $X-$gating variable of I_K with a model formulation that was fairly simple and purely voltage-dependent, and using a square wave approximation of the AP led to the derivation of the iterated map in Eq. (9). However, the

formulations of $[Ca^{2+}]_i$ in the TP04 model are rather complicated and depend on various other model variables including the sarcoplasmic reticulum (SR) Ca^{2+} concentration. A phenomenological model of the effects of ion accumulation on APD was used in Schaeffer *et al.* [28], but due to the complex effects of $[Ca^{2+}]_i$ on APD dynamics in the TP04 model, we must rely on further computer simulation results, which are described in detail below.

We examine the interrelationship between APD and c_{init}, the $[Ca^{2+}]_i$ at the beginning of the AP. There are two things to consider, one is the change in $[Ca^{2+}]_i$ during an AP with a known APD, and the other is the dependence of APD on c_{init}. For the former, we fix square wave APs with a given APD a_1 with a pacing period T until equilibrium has been reached, and then switch to square wave APs with a given APD a_2. A snapshot of this protocol is shown in Fig. 18(a), where $T = 1000$ ms, $a_1 = 350$ ms, and $a_2 = 50$ ms. Before time 0, the system is at equilibrium and the dynamics of $[Ca^{2+}]_i$ (dash-dotted/red) is exactly the same during each AP, with $c_{init} = 0.125$ μM.

After time 0, the APDs switch to the lower duration of $a_2 = 50$ ms, and immediately there is a drop in c_{init} of the successive APs (solid red dots of Fig. 18(a)). Fig. 18(b) shows a time series of c_{init} as a function of beat number, where c_{init} at time 0, in Fig. 18(a), corresponds to the 0th beat. After the APD switch, there is an exponential trend of c_{init} towards a new equilibrium of approximately 0.04 μM. Notice that it takes about 45 beats, or 45 s, for the system to reach this new equilibrium, indicative of very slow $[Ca^{2+}]_i$ dynamics. This is in sharp contrast to the slow $X-$gating variable dynamics in the LR1 model, with a time constant on the order of about 1 s.

Assuming that the time series takes on an exponential trend towards an equilibrium initial $[Ca^{2+}]_i$, c^*, then we have

$$c_{n+1} - c^* = (c_n - c^*) \exp [f(a_n)], \qquad (23)$$

where c_n is the initial $[Ca^{2+}]_i$ of the nth AP, a_n is the APD of the nth AP, and $f(a_n)$ is an APD-dependent function dictating the rate at which the system reaches equilibrium. c^* is also APD-dependent, as shown in Figs. 18(a) and (b). Rearranging Eq. (23) gives

$$c_{n+1} = c_n \exp [f(a_n)] + c^* (1 - \exp [f(a_n)]), \qquad (24)$$

and for simplicity we neglect the $c^* (1 - \exp [f(a_n)])$ term to remove the dependence of c^*. Our justification is that this term is negligible so long as $f(APD) \ll 1$, which with very long time constants is the case as shown in Fig. 18(b). This yields the following simplified iterated map:

$$c_{n+1} = c_n \exp [f(a_n)]. \qquad (25)$$

We next analyze the function $f(a_n)$ using computer simulation results. We use the bifurcation diagram in Fig. 17(c) to pick out pacing periods in chaotic regions that result in multiple (ideally, infinite) APDs. For each

AP, we record the APD and initial $[Ca^{2+}]_i$ of the current AP (c_{init}) as well as of the succeeding AP (c_{init+1}). Eq. (25) gives the relationship $f(a_n) = \log \left(\frac{c_{n+1}}{c_n} \right)$, so we perform a log-transform of the ratios of initial $[Ca^{2+}]_i$, $\log \left(\frac{c_{init+1}}{c_{init}} \right)$. This expression is a measurement of the net cytosolic Ca^{2+} gain from and loss into the extracellular space and the SR during an AP. A value greater than zero is indicative of net $[Ca^{2+}]_i$ gain, and a value less than zero is indicative of net $[Ca^{2+}]_i$ loss. If the value equals zero, then there is no net gain or loss of $[Ca^{2+}]_i$ during an AP, and equilibrium is reached.

The results are shown in Fig. 18(c). The pacing periods $T = 1704, 3600, 5602$, and 7600 ms give rise to chaotic APD dynamics, resulting in hundreds of unique APD values and different values of $\log \left(\frac{c_{init+1}}{c_n} \right)$. The figure shows that, generally speaking, $\log \left(\frac{c_{init+1}}{c_{init}} \right)$ increases as APD increases. In addition, increasing the pacing period T reduces $\log \left(\frac{c_{init+1}}{c_{init}} \right)$. These two results are not surprising. A longer APD results in longer Ca^{2+} influx due to $I_{Ca,L}$, and a longer pacing period, for a fixed APD, results in a longer DI that allows for longer Ca^{2+} efflux due to I_{NCX}. From observation, the dependence of $\log \left(\frac{c_{init+1}}{c_{init}} \right)$ is roughly linear with respect to both APD and T, hence giving the relationship

$$\log \left(\frac{c_{init+1}}{c_{init}} \right) = f(APD) \approx \gamma_a APD - \gamma_T T + \delta, \quad (26)$$

where γ_a and γ_T are the coupling coefficients for APD and T respectively, and δ is a constant. Substituting this expression for f in Eq. (25) gives

$$c_{n+1} = c_n \exp [f(a_n)] = c_n \exp [\gamma_a a_n - \gamma_T T + \delta] \quad (27)$$

We now switch our focus to the dependence of APD on c_{init}. Again, we use the data used to generate the bifurcation diagram in Fig. 17(c), where for each AP we record the APD as well as c_{init}. For all data points with $T > 2000$ ms, we do a scatter plot of APD against c_{init}, and the results are shown in Fig. 18(d). The restriction $T > 2000$ ms avoids any other memory effects and assures that the APD is dependent only on c_{init}. Strikingly, there is a clear one-to-one dependence of APD on c_{init} in which any particular c_{init} gives rise to a unique APD value, without ambiguity. Thus, we may write a functional relationship between APD and c_{init}:

$$APD = g(c_{init}), \qquad (28)$$

so that in the nth AP, the APD a_n depends on the initial $[Ca^{2+}]_i$ c_n via

$$a_n = g(c_n). \qquad (29)$$

And together, Eqs. (27) and (29) give rise to a complete iterated map model:

$$a_n = g(c_n) \qquad (30)$$
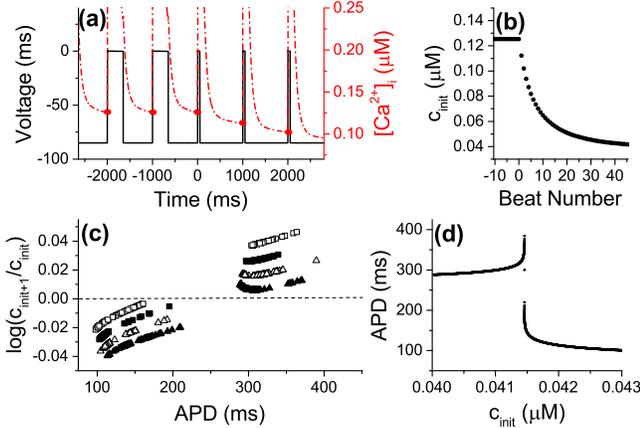$$c_{n+1} = c_n \exp [\gamma_a a_n - \gamma_T T + \delta]. \qquad (31)$$

FIG. 19. Bifurcation of the $Ca^{2+}-$memory map model (Eqs. (30) and (31)), with function g, the APD dependence on c_{init}, the linear interpolant of the data in Fig. 18(d), and parameter values $\gamma_a = 2 \times 10^{-4}\,\mathrm{ms}^{-1}, \gamma_T = 3.625 \times 10^{-6}\,\mathrm{ms}^{-1}$, and $\delta = -0.0275$.

FIG. 18. APD and $[Ca^{2+}]_i$ dynamics of the AP model. **(a)**. Ca^{2+} transients responding to square-wave APs with $T = 1000\,\mathrm{ms}$, with durations switching from APD $= 350\,\mathrm{ms}$ (for all times $t < 0\,\mathrm{ms}$) to APD $= 50\,\mathrm{ms}$ (starting at time $t = 0\,\mathrm{ms}$). **(b)**. Response of c_{init} after the APD switch. **(c)**. Dependence of $\log\left[\frac{c_{init+1}}{c_{init}}\right]$ on APD. The data points were chosen from pacing periods $T = 1704\,\mathrm{ms}$ (open squares), $3600\,\mathrm{ms}$ (filled squares), $5602\,\mathrm{ms}$ (open triangles), $7600\,\mathrm{ms}$ (filled triangles), that result in chaotic behavior resulting in APs with hundreds of unique APDs. **(d)**. Dependence of APD on c_{init}. Data chosen from all APs generating the bifurcation diagram in Fig. 17(c) for $T > 2000\,\mathrm{ms}$.

We refer to this iterated map model as the "$Ca^{2+}-$memory map model." The function g is obtained by linearly interpolating the data in Fig. 18(d). The constants γ_a, γ_T, and δ are obtained from observing the data in Fig. 18(c). We obtain the values $\gamma_a = 2 \times 10^{-4}\,\mathrm{ms}^{-1}, \gamma_T = 3.625 \times 10^{-6}\,\mathrm{ms}^{-1}$, and $\delta = -0.0275$.

As usual, by varying T we create a bifurcation diagram of the $Ca^{2+}-$memory map model, and the result is shown in Fig. 19. The diagram shows stunning similarity to the bifurcation diagram of the AP model shown in Fig. 17(c), revealing numerous period-doubling bifurcation routes to chaos interspersed with periodic windows. In addition, the complete region of instability ranges from about 200 ms to 8500 ms, which is nearly the same as in the AP model.

Fig. 20 compares return maps between the AP model and the $Ca^{2+}-$memory map model (Eqs. (30) and (31)) used to generate the bifurcation in Fig. 19. Fig. 20(a) provides two return maps of the AP model undergoing chaotic APD dynamics with $T = 3250\,\mathrm{ms}$ (black) and $6600\,\mathrm{ms}$ (gray), and Fig. 20(b) are two return maps of the $Ca^{2+}-$memory map model using the same pacing periods $T = 3250\,\mathrm{ms}$ and $6600\,\mathrm{ms}$. Matching the pacing periods between the two graphs, the return maps in the $Ca^{2+}-$memory map model are very similar to the return maps in the AP model. Panel (b) contains more information due to the iterated map being continuous and the chaotic dynamics in the AP model not attaining all
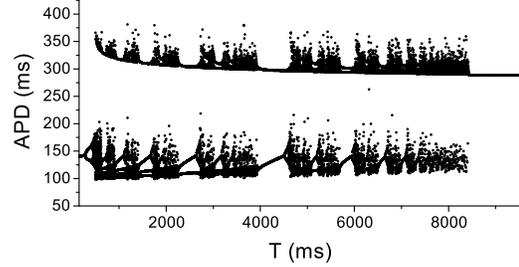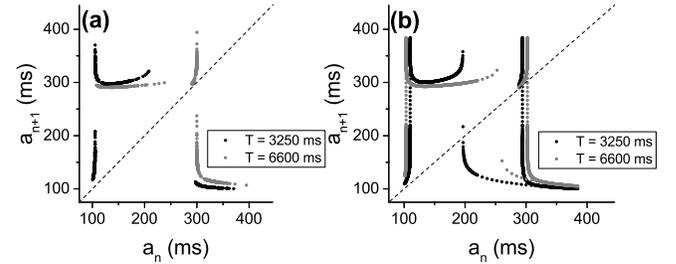

FIG. 20. Comparing return maps between the AP model and $Ca^{2+}-$memory map model (Eqs. (30) and (31)). **(a)**. AP model return maps in chaotic regimes for $T = 3250\,\mathrm{ms}$ (black) and $6600\,\mathrm{ms}$ (gray). **(b)**. Return maps of the $Ca^{2+}-$memory map model for the same pacing periods $T = 3250\,\mathrm{ms}$ (black) and $6600\,\mathrm{ms}$ (gray), where the function g is the linear interpolant of the data in Fig. 18(d), and parameter values $\gamma_a = 2 \times 10^{-4}\,\mathrm{ms}^{-1}, \gamma_T = 3.625 \times 10^{-6}\,\mathrm{ms}^{-1}$, and $\delta = -0.0275$.

possible APDs. For example, for $T = 6600\,\mathrm{ms}$ (the gray points in Fig. 20), in the AP model, APDs below about $a_n = 110\,\mathrm{ms}$ and between $a_n = 230\,\mathrm{ms}$ and $280\,\mathrm{ms}$ do not occur. The return map shows only one discontinuity, or jump between large and small APDs, occurring around $a_n = 300\,\mathrm{ms}$. However, the corresponding return map from the $Ca^{2+}-$memory map model shows two additional discontinuities occurring at $a_n = 100\,\mathrm{ms}$ and $250\,\mathrm{ms}$.

Properties of the $Ca^{2+}-$memory map model incorporating memory effects from $[Ca^{2+}]_i$ accumulation closely match those of the AP model. This provides clear evidence that the $Ca^{2+}-$memory map model sufficiently matches the APD dynamics of the AP model.

3. *Theoretical Analysis and predictions of the $Ca^{2+}-$memory map model*

In the previous section we used the $Ca^{2+}-$memory map model (Eqs. (30) and (31)), in which Eq. (31) is an explicit equation with parameters γ_a, γ_T, T, and δ, but the function g in Eq. (30) was a linear interpolation of data provided by simulations of the AP model. In this

section, we do as before in the case of the $X-$memory map model and set the function g in Eq. (28) as a Hill function of the form $\text{APD} = g(c_{init}) = a_{min} + \frac{a_{max}-a_{min}}{1+\left(\frac{c_{init}}{k_c}\right)^h}$, where a_{min} and a_{max} are the minimum and maximum APDs attainable, k_c is the half-max c_{init}, and h is the Hill coefficient. This gives the following complete iterated map model:

$$a_n = g(c_n) = a_{min} + \frac{a_{max} - a_{min}}{1 + \left(\frac{c_n}{k_c}\right)^h} \tag{32}$$

$$c_{n+1} = f(c_n, a_n) = c_n \exp\left(\gamma_a a_n - \gamma_T T + \delta\right) = H(c_n). \tag{33}$$

Eqs. (32) and (33) together give a complete 1-dimensional map whose steady state stability is determined by the derivative of the function H at steady state:

$$H'(c^*) = [1 + c^* \gamma_a g'(c^*)] e^{\gamma_a g(c^*) - \gamma_T T + \delta}, \tag{34}$$

where c^* is the steady state of H (i.e. $H(c^*) = c^*$). For the period-doubling bifurcation to occur ($H'(c^*) < -1$), it requires a steeply decreasing function g with respect to c_n, i.e., a large negative $g'(c^*)$ is needed so that

$$c^* \gamma_a g'(c^*) < -2 \tag{35}$$

can be satisfied. Increasing γ_a can also potentiate the inequality in Eq. (35) and thus instability. Once Eq. (35) is satisfied, increasing δ or decreasing γ_T will potentiate the instability.

We now examine the model directly by iterating the map in Eqs. (32) and (33) for specific parameter values. Based on simulation results from the AP model shown in Fig. 18, we estimate the parameter values $\gamma_a = 2 \times 10^{-4}\,\text{ms}^{-1}$, $\gamma_T = 3.625 \times 10^{-6}\,\text{ms}^{-1}$, and $\delta = -0.0275$. To model the function g in Eq. (33), we estimate a Hill function that closely matches the dependence of APD on c_{init} from the AP model, as shown in Fig. 18(d). No Hill function will perfectly fit it since the graph is nonmonotonic with a jump discontinuity. Our chosen parameter values are $a_{min} = 125\,\text{ms}$, $a_{max} = 350\,\text{ms}$, $k_c = 4.1456 \times 10^{-2}\,\mu\text{M}$, and $h = 500$. The bifurcation diagram of this model is shown in Fig. 21(a), and shows period-doubling bifurcation routes to enter and exit chaos, similar to the bifurcation diagram of the AP model (Fig. 17(c)) as well as the bifurcation diagram of the $X-$memory map model in the previous section (Fig. 9(f)). The region of instability is between pacing periods $T = 550\,\text{ms}$ and $10\,500\,\text{ms}$, which is roughly similar to that seen in the AP model. In Fig. 21(b) we provide four return maps with different pacing periods. The return maps are very similar to the ones from the $X-$memory map model, shown in Fig. 10(b). An increase in T tends to shift the return map to the right, shifting the fixed point of APD to more positive values.

To confirm our predictions of the effects of γ_T and δ on the stability of the model, we modify these parameters
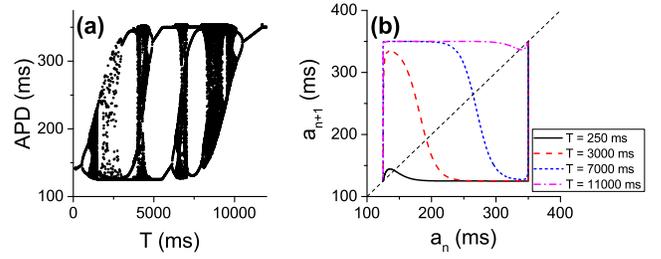

FIG. 21. Dynamics of the $Ca^{2+}-$memory map model (Eqs. (32) and (33)), with parameters $a_{min} = 125\,\text{ms}$, $a_{max} = 350\,\text{ms}$, $k_c = 4.1456 \times 10^{-2}\,\mu\text{M}$, $h = 500$, $\gamma_a = 2 \times 10^{-4}\,\text{ms}^{-1}$, $\gamma_T = 3.625 \times 10^{-6}\,\text{ms}^{-1}$, and $\delta = -0.0275$. **(a)**. Bifurcation diagram. **(b)**. Return maps for pacing periods $T = 250\,\text{ms}$, $3000\,\text{ms}$, $7000\,\text{ms}$, and $11\,000\,\text{ms}$. The dotted/black line is the fixed point line $a_{n+1} = a_n$.

in the $Ca^{2+}-$memory map model using the linear interpolant of the data in Fig. 18(d) to model the function g in Eq. (32). We make the changes $\gamma_T \to 1.25\gamma_T$ and $\delta \to \delta + 0.005$. The results are shown in Fig. 22. Indeed, comparing Fig. 22(a) and (b), there is a shift in the region of instability by about $1380\,\text{ms}$. The left bifurcation points shifts from about $270\,\text{ms}$ to $1650\,\text{ms}$, and the right bifurcation point from about $8430\,\text{ms}$ to $9810\,\text{ms}$. And by increasing γ_T by 25% we expect the left and right bifurcation points to decrease by 20%. Indeed, the left bifurcation point shifts from about $270\,\text{ms}$ to $215\,\text{ms}$ and the right bifurcation point shifts from about $8430\,\text{ms}$ to $6745\,\text{ms}$.

Finally, we return back to the AP model and examine the effects of changing parameters in the model on APD dynamics. Two key regulators of $[Ca^{2+}]_i$ are the L-type Ca^{2+} current, $I_{Ca,L}$, and the Na-Ca exchanger, I_{NCX}. Each have maximum conductance parameters $g_{Ca,L}$ and g_{NCX}, which we change in the model. Fig. 23 shows bifurcation diagrams of (a) control conditions, (b) $g_{Ca,L}$ reduced by 2%, and (c) g_{NCX} reduced by 10%. The diagrams show that the reduction of $I_{Ca,L}$ and I_{NCX} conductance shifts the bifurcation points significantly to the right by about $3500\,\text{ms}$. We currently ignore the left bifurcation point because, in the AP model, many sources could contribute to APD dynamics besides $[Ca^{2+}]_i$ accumulation at such fast pacing periods.

To examine how reducing $I_{Ca,L}$ and I_{NCX} can cause a $3500\,\text{ms}$ shift in the right bifurcation point, we do as before and compare the dependences of $\log\left(\frac{c_{init+1}}{c_{init}}\right)$ to APD, which corresponds to the function f in Eq. (25). To get as many data points as possible, we choose a pacing period $T = 3600\,\text{ms}$ that results in chaotic APD dynamics in control and $I_{Ca,L} \times 0.98$ conditions, and period-3 APD dynamics in the $I_{NCX} \times 0.9$ condition. Fig. 23(d) shows the results. Indeed, the data corresponding to $I_{Ca,L}$ and I_{NCX} reduction lie above the data points under control conditions by about a value of 0.05, which corresponds to an increase in $-\gamma_T T + \delta$ in Eq. (25), so that
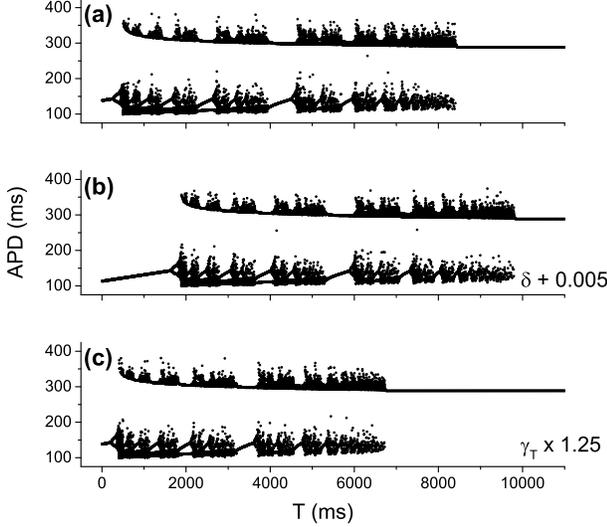
FIG. 22. The effects of δ and γ_T on APD dynamics in the $Ca^{2+}-$memory map model (Eqs. (30) and (31)). **(a)**. Bifurcation under control conditions, using the linear interpolant of the curve in Fig. 18(d) for g and other parameters $\gamma_a = 2.4 \times 10^{-4}\,\mathrm{ms}^{-1}, \gamma_T = 3.625 \times 10^{-6}\,\mathrm{ms}^{-1}$, and $\delta = -0.0275$. **(b)**. Bifurcation diagram with $\delta \rightarrow \delta + 0.005 = -0.0225$. **(c)**. Bifurcation diagram with $\gamma_T \rightarrow 2\gamma_T = 7.25 \times 10^{-6}\,\mathrm{ms}^{-1}$.

either δ increases, γ_T decreases, or a combination of both. In either case, the theoretical analysis suggests that decreasing $I_{\mathrm{Ca,L}}$ or I_{NCX} causes an increase in δ and/or a decrease in γ_T, which shifts the right bifurcation point to the right, just as we see in the simulation results.

4. EAD-induced complex APD dynamics in the presence of $[Ca^{2+}]_i$ accumulation

Similar to the case of the LR1 model, we also generate EADs in the TP04 model in the absence of I_{to} (Fig. 24(a)). To do so, we set the maximum conductances of $I_{Ca,L}, I_{Kr}$, and I_{Ks} to be $g_{\mathrm{Ca,L}} = 6 \times 10^{-4}\,\mathrm{mS/cm}^2, g_{kr} = 0.01\,\mathrm{mS/cm}^2$, and $g_{ks} = 0.036\,\mathrm{mS/cm}^2$, and introduce a late Na^+ current by performing the following changes to the formulations of the steady-state $h-$ and $j-$gates in I_{Na}:

$$h_\infty = \gamma + (1 - \gamma)\overline{h_\infty}$$
$$j_\infty = \gamma + (1 - \gamma)\overline{j_\infty}, \tag{36}$$

where $\overline{h_\infty}$ and $\overline{j_\infty}$ are the steady state formulations of the two gates in the TP04 model, and γ is a "pedestal" parameter that determines to what extent the $h-$ and $j-$ gates deactivate. Here, we set $\gamma = 0.01$.

Fig. 24(b) is a bifurcation diagram against the pacing period T from the simulation of the TP04 model. Between each transition leading to an extra EAD (i.e. 0 EADs to 1 EAD, 1 EAD to 2 EADs, etc.), there is a
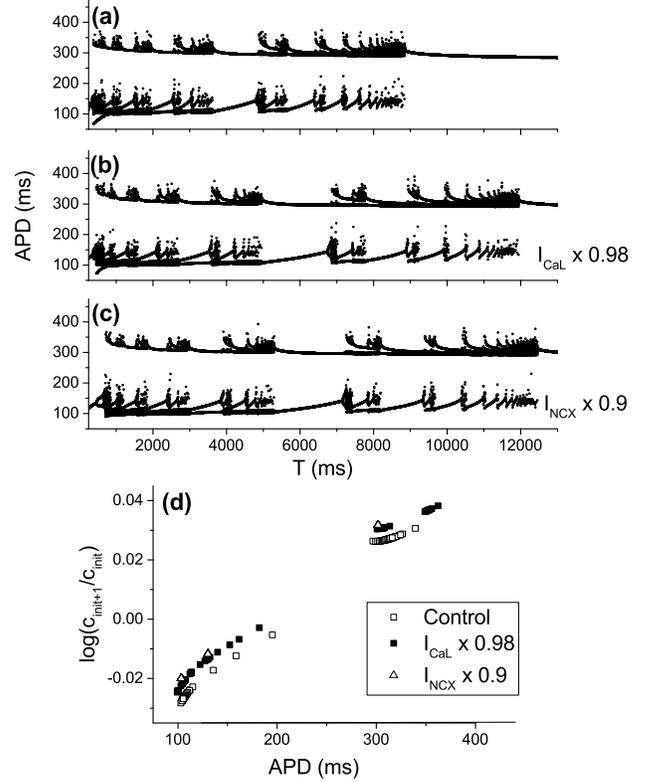

FIG. 23. The effects of changing $I_{Ca,L}$ and I_{NCX} on the APD dynamics of the AP model. **(a)**. Bifurcation diagram under control conditions. **(b)**. Bifurcation diagram when $g_{Ca,L}$ is reduced by 2%. **(c)**. Bifurcation diagram when g_{NCX} is reduced by 10%. **(d)**. The effects of reducing $I_{Ca,L}$ by 2% and I_{NCX} by 10% on the dependence of $\log\left(\frac{c_{init+1}}{c_{init}}\right)$ on APD. In each case, simulations use a pacing period $T = 3600\,$ms, where Control and $I_{Ca,L} \times 0.98$ conditions result in chaotic APD dynamics and the $I_{NCX} \times 0.9$ condition results in period-3 APD dynamics.

period doubling bifurcation route to enter chaos as T increases. Fig. 24(c) shows a close-up of the bifurcation diagram around the first transition between 0 EADs and 1 EAD, more clearly illustrating period doubling leading to chaos.

We calculate the S1S2 APD restitution curves for two different S1 pacing periods, $T_{S1S1} = 2000\,$ms and $6000\,$ms (Fig. 25(a)). Just as in the LR1 model with EADs, the S1S2 restitution curves show staircase dependences of APD against DI. The bifurcation diagrams obtained using the S1S2 APD restitution curves and Eq. (2) are given in Figs. 25(b) and (d), with corresponding close-ups around the first bifurcation points in Figs. 25(c) and (e), respectively. The bifurcation diagrams differ largely from those from the AP model, indicating that APD restitution alone cannot capture the complex excitation dynamics.

We then plot APD versus c_{init} and $\log\left(\frac{c_{init+1}}{c_{init}}\right)$ versus

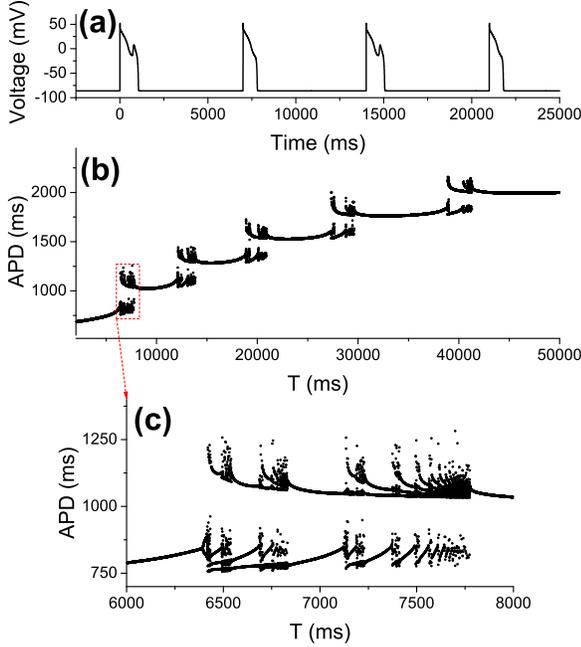FIG. 24. Complex APD dynamics induced by EADs in the TP04 model, with $g_{Ca,L} = 6 \times 10^{-4}\,\mathrm{mS/cm^2}, g_{kr} = 0.01\,\mathrm{mS/cm^2}, g_{ks} = 0.0036\,\mathrm{mS/cm^2}$, and $\gamma = 0.01$ in Eq. (36). (a). APs showing EAD alternans, $T = 7000\,\mathrm{ms}$. (b). Bifurcation diagram of the AP model. (c). Close-up of the bifurcation diagram around the first bifurcation point, transitioning from no EADs to one EAD in the AP.
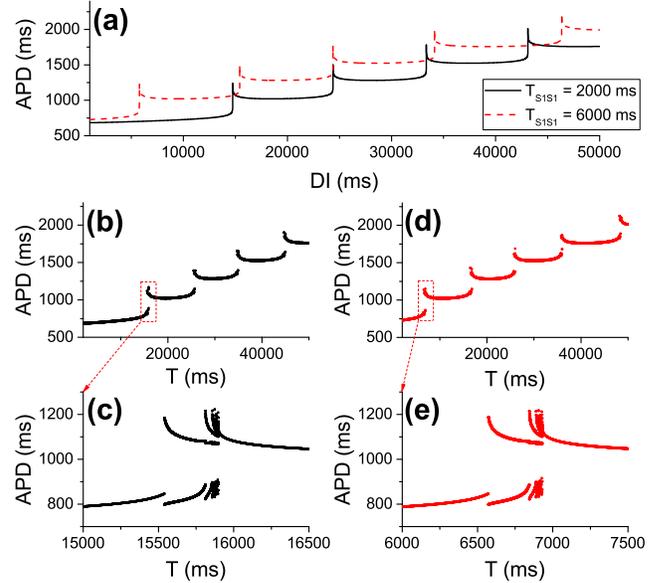

FIG. 25. Bifurcation diagrams from the APD-restitution map model (Eq. (2)) and S1S2 APD restitution curves from the TP04 model in the context of long QT syndrome. (a). S1S2 restitution curves for S1 pacing periods $T_{S1S1} = 2000\,\mathrm{ms}$ (solid/black) and $6000\,\mathrm{ms}$ (dashed/red). (b). Bifurcation diagram of the APD-restitution map model (Eq. (2)) using the solid/black trace in (a). (c). Close-up of the bifurcation diagram in (b) around the first bifurcation point. (d). Bifurcation of the APD-restitution map model (Eq. (2)) using the dashed/red trace in (a). (e). Close-up of the bifurcation diagram in (d) around the first bifurcation point.

APD from the AP model the same way as we did in the I_{to} case (Figs. 26(a) and (b)). Using these functions and the $\mathrm{Ca}^{2+}-$memory map model (Eqs. (30) and (31)), we obtain a bifurcation diagram (Fig. 26(c)) which is nearly identical to the one obtained from the AP model (Fig. 24(c)). This shows that the memory from $[\mathrm{Ca}^{2+}]_i$ accumulation plays an important role in generating the complex APD dynamics induced by the occurrence of EADs in the AP model.

IV. DISCUSSION AND CONCLUSIONS

In this study, we investigated the effects of short-term cardiac memory on excitation dynamics under two diseased conditions, early repolarization syndrome [47] and long QT syndrome [51]. The memory originates from two sources, slow ion channel recovery and slow $[\mathrm{Ca}^{2+}]_i$ accumulation. We show that contrary to many previous studies which have shown that memory suppresses dynamical instabilities [25–27, 29–37], under these diseased conditions, memory can induce or potentiate complex excitation dynamics, including chaos. In addition to memory, the all-or-none behaviors (dome vs. no dome or EAD vs. no EADs) in the diseased conditions, which result in steeply changing APD restitution curves, are also key to the genesis of the complex APD dynamics. We

developed new iterated map models that properly incorporate memory from the two different sources, which can well describe the complex dynamics and recapitulate the bifurcation sequences from the AP models. Using the iterated map models, we unraveled the mechanisms underlying memory-induced chaos and complex APD dynamics induced by I_{to} or EADs.

The role of chaos in the genesis and maintenance of cardiac arrhythmias has been investigated previously [13, 65, 66]. Different mechanisms of chaos and complex excitation dynamics have been demonstrated in cardiac myocytes. In this study, we reveal a novel mechanism of chaos of cardiac excitation, which may provide further understanding of the role of chaos in arrhythmogenesis in the presence of short-term cardiac memory.

In this study, we investigated the effects of memory originating from slow recovery of ion channels and slow accumulation of $[\mathrm{Ca}^{2+}]_i$. We fixed $[\mathrm{Na}^+]_i$ and $[\mathrm{K}^+]_i$ in our simulations in order to avoid memory effects from slow accumulation of these ions. However, it is well known that, in particular, $[\mathrm{Na}^+]_i$ accumulates very slowly, and thus it can impact the APD dynamics in an even longer time scale, i.e., longer-term memory effect. These effects have been already investigated in recent simulation studies [67, 68]. It will be of importance to
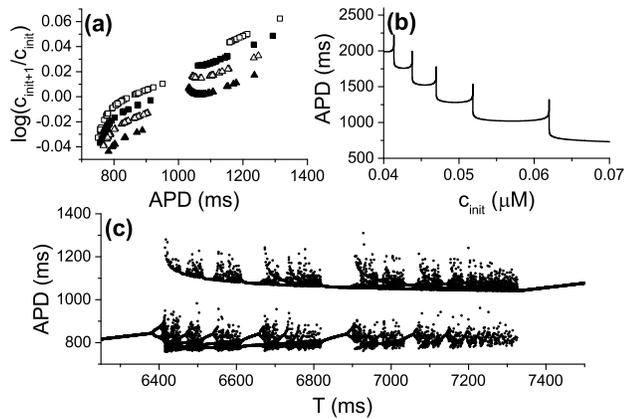
FIG. 26. APD dynamics predicted by the $Ca^{2+}-$memory map model (Eqs. (30) and (31)) in the presence of EADs. **(a)**. Plots of $\log\left(\frac{c_{init+1}}{c_{init}}\right)$ vs. APD from the AP model for 4 different pacing periods leading to chaotic EAD dynamics, $T = 6430\,\text{ms}$ (open squares), $6805\,\text{ms}$ (filled squares), $7190\,\text{ms}$ (open triangles), and $7710\,\text{ms}$ (filled triangles). **(b)**. Plot of APD vs. c_{init} in the AP model. **(c)**. Bifurcation diagram of the $Ca^{2+}-$memory map model (Eqs. (30) and (31)). The paramters in Eq. (31) were chosen to be $\gamma_a = 1.2 \times 10^{-4}\,\text{ms}^{-1}, \gamma_T = 2.5 \times 10^{-5}\,\text{ms}^{-1}$, and $\delta = 0.05845$, based on approximating the data in panel (a). The function g in Eq. (31) is the linear interpolant of the data in panel (b).

develop an improved iterated map model that incorporates the memory caused by slow $[Na^+]_i$ accumulation, which is our next task of revealing the mechanisms of short-term cardiac memory on excitation dynamics.

Finally, we would like to point out that the mechanistic insights gained from the present study may not only be limited to complex ecitation dynamics in cardiac myocytes, but also to those in other electrically excitable cells. For example, the bursting dynamics in neurons [69–72] and pancreatic $\beta-$cells [73] are irregular, which can result from either random ion channel openings or dynamical chaos. Since the bursting dynamics are also governed by fast-slow dynamics [62, 73–76] similar to the EAD dynamics in cardiac myocytes, the same mechanism of memory-induced chaos may be applicable to irregular bursting dynamics in these cases.

ACKNOWLEDGMENTS

[1] L. Glass, Physics Today **49**, 40 (1996).
[2] Z. Qu and J. N. Weiss, Annual review of physiology **77**, 29 (2015).
[3] D. P. Zipes and H. J. Wellens, Circulation **98**, 2334 (1998).
[4] T. Krogh-Madsen and D. J. Christini, Annual review of biomedical engineering **14**, 179 (2012).
[5] A. Karma, Annu. Rev. Condens. Matter Phys. **4**, 313 (2013).
[6] Z. Qu, G. Hu, A. Garfinkel, and J. Weiss, Physics Reports **543**, 61 (2014).
[7] J. Nolasco and R. Dahlen, Journal of Applied Physiology **25**, 191 (1968).
[8] M. Guevara, L. Glass, and A. Shrier, Science **214**, 1350 (1981).
[9] M. Guevara, G. Ward, A. Shrier, and L. Glass, IEEE Computational Cardiology **562**, 167 (1984).
[10] D. Chialvo, R. Gilmour Jr, and J. Jalife, Nature **343**, 653 (1990).
[11] H. S. Karagueuzian, S. S. Khan, K. Hong, Y. Kobayashi, T. Denton, W. J. Mandel, and G. A. Diamond, Circulation **87**, 1661 (1993).
[12] M. Watanabe, N. Otani, and R. Gilmour Jr, Circulation Research **76**, 915 (1995).
[13] D. Sato, L.-H. Xie, A. Sovari, D. Tran, N. Morita, F. Xie, H. Karagueuzian, A. Garfinkel, J. Weiss, and Z. Qu, Proceedings of the National Academy of Sciences of the United States of America **106**, 2983 (2009).
[14] Y. Shiferaw, D. Sato, and A. Karma, Physical Review E

[15] V. Elharrar and B. Surawicz, American Journal of Physiology - Heart and Circulatory Physiology **244**, H782 (1983).
[16] M. R. Franz, J. Schaefer, M. Schöttler, W. A. Seed, and M. I. Noble, Circulation Research **53**, 815 (1983).
[17] R. B. Robinson, P. A. Boyden, B. F. Hoffman, and K. W. Hewett, American Journal of Physiology-Heart and Circulatory Physiology **253**, H1018 (1987).
[18] S. Dilly and M. Lab, The Journal of Physiology **402**, 315 (1988).
[19] J. M. Morgan, D. Cunningham, and E. Rowland, British heart journal **67**, 42 (1992).
[20] A. Vinet, D. Chialvo, D. Michaels, and J. Jalife, Circulation Research **67**, 1510 (1990).
[21] A. Karma, Chaos: An Interdisciplinary Journal of Nonlinear Science **4**, 461 (1994).
[22] Z. Qu, Y. Shiferaw, and J. Weiss, Physical Review E **75**, 011927 (2007).
[23] M. Franz, C. Swerdlow, L. Liem, and J. Schaefer, Journal of Clinical Investigation **82**, 972 (1988).
[24] S. Kalb, H. Dobrovolny, E. Tolkacheva, S. Idriss, W. Krassowska, and D. Gauthier, Journal of Cardiovascular Electrophysiology **15**, 1 (2004).
[25] S. Kalb, E. Tolkacheva, D. Schaeffer, D. Gauthier, and W. Krassowska, Chaos **15**, 023701 (2005).
[26] D. R. Chialvo, D. C. Michaels, and J. Jalife, Circulation Research **66**, 525 (1990).
[27] J. J. Fox, E. Bodenschatz, and J. Robert F. Gilmour,

71, 021903 (2005).

Physical Review Letters **89** (2002), 10.1103/PhysRevLett.89.138101.

[28] D. G. Schaeffer, J. W. Cain, D. J. Gauthier, S. S. Kalb, R. A. Oliver, E. G. Tolkacheva, W. Ying, and W. Krassowska, Bulletin of mathematical biology **69**, 459 (2007).

[29] N. Otani and R. Gilmour Jr, Journal of Theoretical Biology **187**, 409 (1997).

[30] E. G. Tolkacheva, D. G. Schaeffer, D. J. Gauthier, and W. Krassowska, Phys. Rev. E **67**, 031904 (2003).

[31] J. Fox, M. Riccio, P. Drury, A. Werthman, and R. Gilmour Jr., New Journal of Physics **5**, 101 (2003).

[32] E. G. Tolkacheva, M. M. Romeo, M. Guerraty, and D. J. Gauthier, Phys. Rev. E **69**, 031904 (2004).

[33] E. Cherry and F. Fenton, American Journal of Physiology **286**, H2332 (2004).

[34] A. Baher, Z. Qu, A. Kayatdavoudi, S. Lamp, M.-J. Yang, F. Xie, S. Turner, A. Garfinkel, and J. Weiss, American Journal of Physiology - Heart and Circulatory Physiology **292**, H180 (2007).

[35] A. Gizzi, E. Cherry, R. F. Gilmour Jr, S. Luther, S. Filippi, and F. H. Fenton, Frontiers in physiology **4**, 71 (2013).

[36] S. Mironov, J. Jalife, and E. G. Tolkacheva, Circulation **118**, 17 (2008), http://circ.ahajournals.org/content/118/1/17.full.pdf.

[37] N. Wei, Y. Mori, and E. G. Tolkacheva, Journal of Theoretical Biology **367**, 21 (2015).

[38] J. Landaw, A. Garfinkel, J. N. Weiss, and Z. Qu, Phys. Rev. Lett. **118**, 138101 (2017).

[39] J. L. Greenstein, R. Wu, S. Po, G. F. Tomaselli, and R. L. Winslow, Circulation Research **87**, 1026 (2000), http://circres.ahajournals.org/content/87/11/1026.full.pdf.

[40] X. Sun and H.-S. Wang, The Journal of physiology **564**, 411 (2005).

[41] M. Dong, X. Sun, A. A. Prinz, and H.-S. Wang, American Journal of Physiology-Heart and Circulatory Physiology **291**, H631 (2006).

[42] A. Lukas and C. Antzelevitch, Circulation **88**, 2903 (1993).

[43] B. Hopenfeld, Heart Rhythm **3**, 345 (2006).

[44] A. Maoz, T. Krogh-Madsen, and D. J. Christini, Heart Rhythm **6**, 813 (2009).

[45] I. R. Cantalapiedra, A. Peñaranda, L. Mont, J. Brugada, and B. Echebarria, Journal of theoretical biology **259**, 850 (2009).

[46] Z. Qu, Y. Xie, A. Garfinkel, and J. N. Weiss, Frontiers in physiology **1**, 154 (2010).

[47] C. Antzelevitch and G.-X. Yan, Heart Rhythm **12**, 1852 (2015).

[48] C. T. January and A. Moscucci, Annals of the New York Academy of Sciences **644**, 23 (1992).

[49] Z. Qu, L.-H. Xie, R. Olcese, H. S. Karagueuzian, P.-S. Chen, A. Garfinkel, and J. N. Weiss, Cardiovascular research **99**, 6 (2013).

[50] I. Goldenberg, W. Zareba, and A. J. Moss, Current problems in cardiology **33**, 629 (2008).

[51] D. Roden, Journal of Internal Medicine **259**, 59 (2006).

[52] Q. Wang, J. Shen, I. Splawski, D. Atkinson, Z. Li, J. L. Robinson, A. J. Moss, J. A. Towbin, and M. T. Keating, Cell **80**, 805 (1995).

[53] C. E. Clancy and Y. Rudy, Cardiovascular research **50**, 301 (2001).

[54] G. F. Tomaselli and E. Marbán, Cardiovascular research **42**, 270 (1999).

[55] C.-H. Luo and Y. Rudy, Circulation Research **68**, 1501 (1991).

[56] K. ten Tusscher, D. Noble, P. Noble, and A. Panfilov, American Journal of Physiology - Heart and Circulatory Physiology **286**, H1573 (2004).

[57] A. Mahajan, Y. Shiferaw, D. Sato, A. Baher, R. Olcese, L.-H. Xie, M.-J. Yang, P.-S. Chen, J. G. Restrepo, A. Karma, *et al.*, Biophysical journal **94**, 392 (2008).

[58] M. C. Sanguinetti and N. K. Jurkiewicz, The Journal of general physiology **96**, 195 (1990).

[59] J. Zeng, K. R. Laurita, D. S. Rosenbaum, and Y. Rudy, Circulation Research **77**, 140 (1995).

[60] J. Silva and Y. Rudy, Circulation **112**, 1384 (2005).

[61] P. J. Schwartz, Journal of internal medicine **259**, 39 (2006).

[62] D. X. Tran, D. Sato, A. Yochelis, J. N. Weiss, A. Garfinkel, and Z. Qu, Physical Review Letters **102**, 258103 (2009).

[63] D. Sato, L.-H. Xie, T. P. Nguyen, J. N. Weiss, and Z. Qu, Biophysical journal **99**, 765 (2010).

[64] G. M. Faber and Y. Rudy, Biophysical journal **78**, 2392 (2000).

[65] Y. Xie, G. Hu, D. Sato, J. N. Weiss, A. Garfinkel, and Z. Qu, Physical Review Letters **99**, 118101 (2007).

[66] Z. Qu, Progress in biophysics and molecular biology **105**, 247 (2011).

[67] Y. Xie, Z. Liao, E. Grandi, Y. Shiferaw, and D. M. Bers, Circulation: Arrhythmia and Electrophysiology , CIRCEP (2015).

[68] T. Krogh-Madsen and D. J. Christini, Chaos: An Interdisciplinary Journal of Nonlinear Science **27**, 093907 (2017).

[69] J. Rinzel and G. B. Ermentrout, Methods in neuronal modeling **2**, 251 (1998).

[70] M. Rabinovich and H. Abarbanel, Neuroscience **87**, 5 (1998).

[71] A. L. Shilnikov and N. F. Rulkov, International Journal of Bifurcation and Chaos **13**, 3325 (2003).

[72] S. Achuthan and C. C. Canavier, Journal of Neuroscience **29**, 5218 (2009).

[73] J. P. Keener and J. Sneyd, *Mathematical Physiology* (Springer, New York, 1998).

[74] C. A. D. Negro, C.-F. Hsiao, S. H. Chandler, and A. Garfinkel, Biophysical Journal **75**, 174 (1998).

[75] E. M. Izhikevich, International Journal of Bifurcation and Chaos **10**,

[76] A. Shilnikov, R. L. Calabrese, and G. Cymbalyuk, Phys. Rev. E **71**, 056214 (2005).